



Progress in atomic layer deposition of metal oxides for efficient and stable perovskite solar cells

Pil Ju Park¹, Hae Jin Jo², Sang Mok Han², Young Ju Kim², Soo Young Kim¹

Keywords:

Perovskite solar cells, atomic layer deposition, metal oxides, interface engineering, defect passivation, charge transport, stability

Citation: Park, P. J.; Jo, H. J.; Han, S. M.; Kim, Y. J.; Kim, S. Y. Progress in atomic layer deposition of metal oxides for efficient and stable perovskite solar cells. *Microstructures* 2026, 6, 2026040. <https://dx.doi.org/10.20517/microstructures.2025.138>

Received: 1 Oct 2025

First Decision: 6 Nov 2025

Revised: 21 Nov 2025

Accepted: 22 Dec 2025

Published: 10 Apr 2026

Academic Editors:

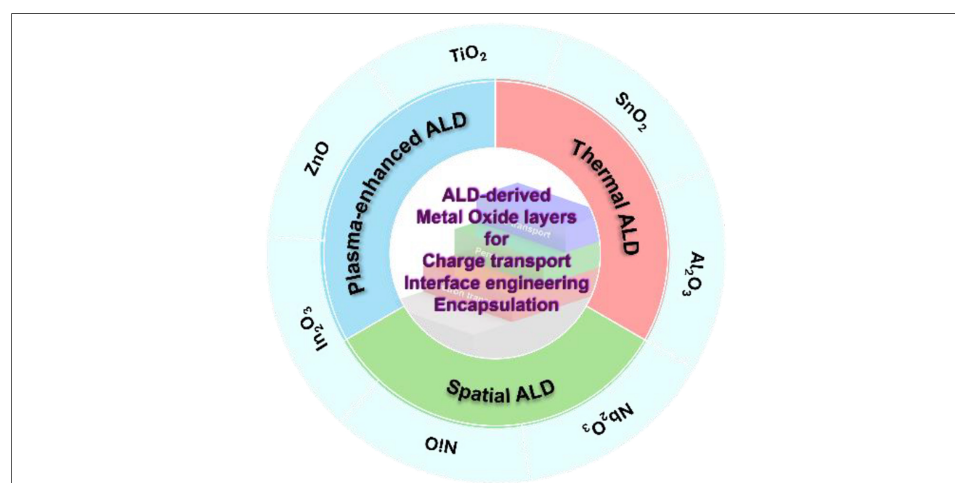
Dae-Yong Jeong, Zhihua Sun

Copy Editor:

Fangling Lan

Production Editor:

Fangling Lan



Abstract

Perovskite solar cells (PSCs) are widely recognized as one of the most promising candidates for next-generation photovoltaics (PV), attributed to their outstanding power conversion efficiency and easily adjustable bandgap. Nevertheless, their practical commercialization remains challenging due to inherent material instabilities and rapid degradation triggered by exposure to moisture, oxygen, ultraviolet light, and thermal stress. In response, atomic layer deposition (ALD) has gained prominence as an advanced thin-film deposition technique, offering atomic-level precision and enabling the fabrication of uniform, conformal, and defect-minimized metal oxide (MO) layers. The ALD MOs serve versatile roles as charge transport layers, interfacial passivation coatings, and encapsulation barriers, collectively enhancing device performance, mechanical integrity, and operational durability. This review highlights the working mechanism of ALD, structural features of PSCs, and key strategies that leverage ALD-grown MOs to address efficiency loss and instability issues. Specific focus is given to defect passivation and protection against environmental factors. Moreover, challenges including precursor optimization, process compatibility with PSC architectures, and cost considerations are examined, along with future perspectives for industrial translation. Finally, the integration of ALD MOs holds strong potential to deliver the stability, efficiency, and scalability



¹Department of Materials Science and Engineering, Korea University, Seoul 02841, Republic of Korea.

²Korea Institute of Geoscience and Mineral Resources 905 Yeongilman-daero, Heunghae-eup, Buk-gu, Pohang-si, Gyeongsangbuk-do 37559, Republic of Korea.

Correspondence to: Dr. Young Ju Kim, Korea Institute of Geoscience and Mineral Resources 905 Yeongilman-daero, Heunghae-eup, Buk-gu, Pohang-si, Gyeongsangbuk-do 37559, Republic of Korea. E-mail: kyjp7272@kigam.re.kr; Prof. Soo Young Kim, Department of Materials Science and Engineering, Korea University, Seoul 02841, Republic of Korea. E-mail: sooyoungkim@korea.ac.kr

essential for the industrial application of PSCs in sustainable PV technologies.

INTRODUCTION

Global industrialization powered by fossil fuels has driven significant economic growth, yet the resulting greenhouse-gas emissions have accelerated climate change. In response, international initiatives such as the Paris Agreement have emphasized carbon neutrality and stimulated a broad shift toward renewable and low-carbon energy systems^[1–3]. Among various sustainable technologies, solar energy has gained particular importance due to its abundance and scalability. Photovoltaics (PVs) that convert sunlight directly into electricity represent a central component of this transition^[4,5].

Crystalline silicon (c-Si) solar cells currently dominate the PV market due to their high efficiency and long-term reliability. Owing to decades of accumulated research and development, Si PVs have achieved both high power conversion efficiency (PCE) and long-term reliability, with stable efficiencies exceeding 20% in practice^[6,7]. However, their indirect bandgap, high-temperature wafer processing, and mechanical rigidity limit further cost reduction and hinder applications in emerging flexible or lightweight devices^[8].

A wide range of inorganic and organic materials have been investigated. Thin-film solar cells such as CIGS ($\text{Cu}(\text{In,Ga})\text{Se}_2$), CdTe, and CZTS ($\text{Cu}_2\text{ZnSnS}_4$) initially attracted significant attention due to their excellent light-absorbing properties and relatively simple fabrication processes^[9–13]. However, challenges including reliance on scarce elements, toxicity, and limited long-term stability have hindered their large-scale commercialization^[14]. Organic and polymer-based solar cells, on the other hand, offer the advantages of low-cost and low-temperature solution processing, yet their inherently limited charge-transport properties and modest optoelectronic performance have prevented them from matching the competitiveness of silicon photovoltaics^[15–18].

Organic-inorganic halide perovskites first reported by Miyasaka's group in 2009 have emerged as a highly promising class of next-generation photoabsorber materials, demonstrating remarkable progress over the past decade^[19–21]. Perovskite solar cells (PSCs) combine several unique advantages not typically offered by conventional semiconductors, including a strong optical absorption coefficient, long charge diffusion lengths, bandgap tuning via compositional engineering, and intrinsic defect tolerance^[22–24]. Since the initial report, in which a PCE of 3.9% was achieved, PSCs have rapidly advanced to exceed 27% within just over a decade, approaching and even surpassing the performance of c-Si^[25,26]. The facile bandgap tunability of halide perovskites further enables integration into tandem architectures with Si solar cells, while low-cost solution-based processing allows scalable large-area fabrication^[27–30]. Owing to these attributes, PSCs are now recognized in academic research as one of the leading candidates for next-generation photovoltaic technologies.

However, the most critical obstacle hindering the commercialization of PSCs lies in instability. Composed of weak ionic bonds, the perovskite crystal lattice is inherently fragile, and readily undergoes degradation when exposed to moisture, oxygen, ultraviolet (UV) radiation, and thermal stress^[31–35]. In particular, moisture disrupts the ionic bonding within the lattice, leading to irreversible structural collapse, while oxygen and UV light trigger photocatalytic oxidation reactions that interfere with charge transport pathways^[36,37]. As a result, maintaining reliable performance over extended periods remains highly challenging. Besides, solution based thin-film fabrication techniques such as spin coating are highly sensitive to external parameters including humidity, temperature, and solvent evaporation rate, making it difficult to achieve uniformity and reproducibility^[38–41]. Unavoidably, the microscopic pinholes and defects are introduced, thereby performance

losses become more pronounced as device areas scale up. Although various mitigation strategies such as interface engineering and additive incorporation have been explored, fundamental limitations still persist^[42–45].

To overcome the limitations of solution-based processes, vacuum deposition techniques have been explored as alternative routes for thin-film fabrication^[46]. High-quality film deposition is facilitated in a vacuum environment, where the attenuation of impurity concentrations and the exclusion of external contaminants are achieved. Accordingly, vacuum deposition techniques such as electron-beam evaporation (EBE), thermal evaporation (TE), and chemical vapor deposition (CVD) have already been applied to PSC fabrication with notable success^[47–50]. Nevertheless, challenges remain for film quality and large-scale commercialization due to the high cost of equipment, complex process control requirements, and the limited availability of suitable precursors^[51,52]. Recently, atomic layer deposition (ALD) has emerged as one of the most promising approaches for enhancing PSC performance^[53,54]. ALD is a vapor-phase thin-film deposition technique based on self-limiting surface reactions, which allows precise control of thickness at the atomic scale. Furthermore, it provides excellent uniformity and conformality even on complex or porous surfaces, thereby enabling the fabrication of pinhole-free films. This capability plays a critical role not only in improving device performance but also in ensuring long-term operational stability^[55,56]. In particular, metal oxide (MO) layers deposited via ALD play a pivotal role in addressing the structural and chemical vulnerabilities of PSCs^[57,58]. MOs are composed of transition metals bonded with oxygen and can exhibit diverse electronic properties such as insulating, n-type or p-type semiconducting behavior, depending on their bandgap, oxygen vacancy concentration, and crystal structure^[59]. On this basis, high-purity and defect-free MOs prepared by ALD can be employed within PSCs for a variety of functional roles. Furthermore, MOs possess excellent thermal and chemical stability, which enables resistance against external factors including moisture, heat, and oxygen^[60,61]. The robust mechanical properties also ensure reliable performance when integrated with flexible substrates. Consequently, MOs not only contribute to extending device lifetimes but also demonstrate significant potential for applications in wearable electronics.

This review focuses on strategies to simultaneously enhance the efficiency and stability of PSCs through the application of MO layers fabricated via ALD. It begins by introducing the fundamental mechanisms and process characteristics of ALD, followed by a systematic analysis of the structural features of PSCs and the intrinsic instabilities of their constituent materials. Subsequently, representative cases of ALD MO thin film and their corresponding effects are summarized, with particular emphasis on approaches to overcome environmental stress factors and intrinsic degradation pathways. The review then provides an in-depth discussion of the synergistic effects enabled by the incorporation of ALD-derived MO layers, along with process optimization strategies, prospects for large-area fabrication, and pathways toward industrial-scale implementation. Finally, the remaining challenges that should be addressed for commercialization are highlighted, including precise control of film properties, process compatibility, cost-effectiveness, and scalable manufacturing infrastructure. Overcoming the intrinsic instabilities of PSCs and establishing efficient and sustainable PV systems will require the strategic design and implementation of ALD-based MO layers. By comprehensively addressing these technical challenges, this review aims to provide a roadmap for the stable and sustainable advancement of PSCs by ALD MO [Figure 1].

WORKING PRINCIPLES AND KEY FEATURES OF ALD IN PSC

Minimizing efficiency losses and degradation in PSCs requires precise defect management and effective suppression of degradation pathways. ALD has emerged as a promising technique capable of meeting these demands and has already been utilized in a variety of photovoltaic technologies, including perovskite, Si, III-V, CdTe, CIGS, organic, and dye-sensitized solar cells (DSSCs)^[62–64]. Owing to its suitability for depositing a wide range of thin films including MOs and nitrides, ALD offers significant advantages for device

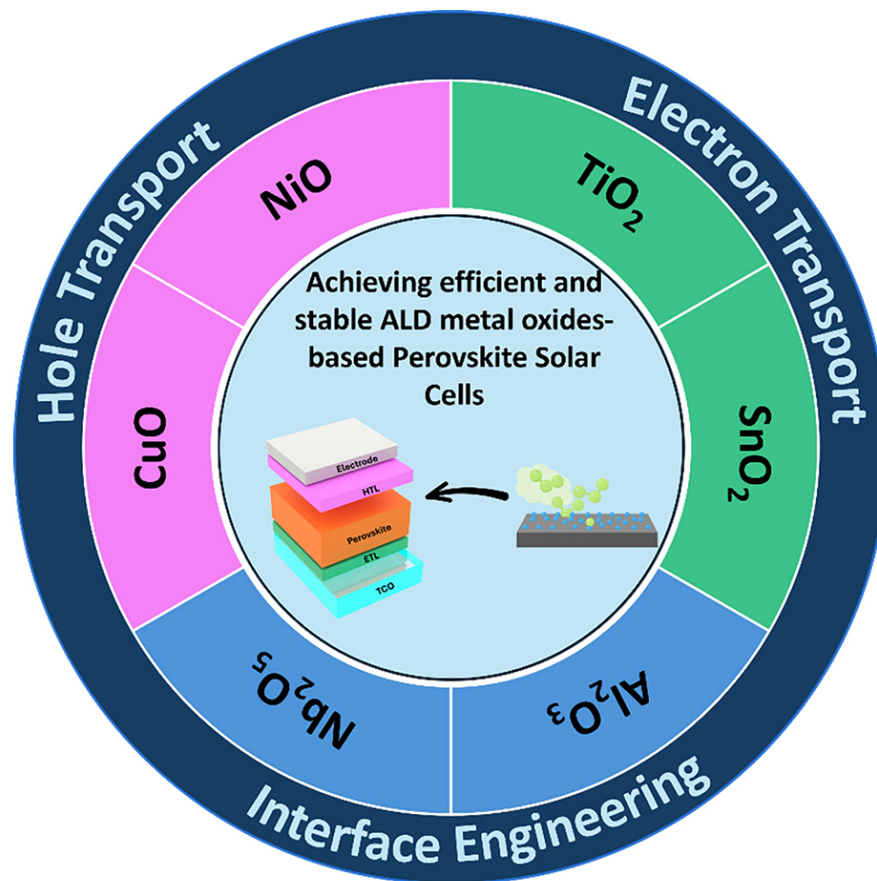


Figure 1. Schematic illustration of ALD MO-based PSC system for improving PCE and stability.

integration^[65]. It is crucial to recognize that successful application of ALD in PSCs necessitates a thorough understanding of the process sequence and approaches specifically tailored to the intrinsic characteristics of PSCs. In this section, we first describe the fundamental mechanisms of ALD and the perovskite photovoltaic system, and then provide a comprehensive discussion of ALD MO for each device component.

ALD fundamentals and process framework

ALD is a sophisticated thin-film deposition technique that relies on self-limiting reactions between precursors and substrate surfaces. This system enables the growth of ultrathin and highly uniform films with atomic-scale thickness control, while also ensuring conformality on substrates with complex surface geometries^[66–68]. The basic protocol of ALD process consists of four sequential steps that together form one cycle, illustrated in Figure 2. First, precursors such as an organometallic compound are introduced into the evacuated reaction chamber and pulsed onto the substrate where they adsorb. The primary adsorption mechanism in ALD is chemisorption, where chemical bonds form between the precursor and reactive surface sites, in contrast to the weaker physisorption governed by van der Waals interactions or hydrogen bonding^[69]. Once the surface is saturated with the precursor, the reaction ceases, demonstrating the self-limiting nature of ALD^[70,71]. The chamber is then purged with an inert gas to remove unreacted precursors and volatile by-products. In the next, oxidizing agent as a second precursor is pulsed into the chamber to react with the chemisorbed species. This forms the desired thin film material while simultaneously regenerating reactive surface sites for the next cycle^[72]. By repeating these steps, the film thickness can be precisely controlled.

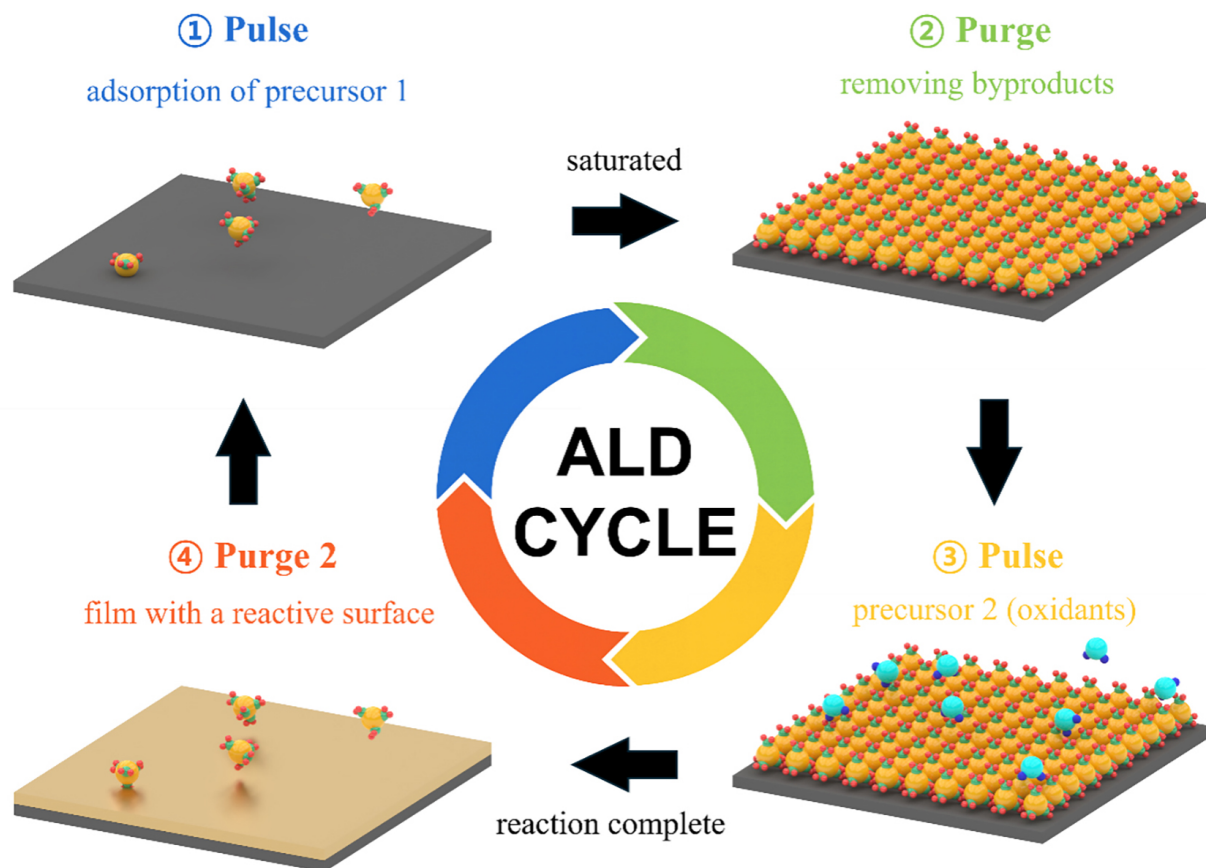


Figure 2. Schematic illustration of ALD process.

ALD offers a clear advantage in conformality compared with solution-based processes and other vapor deposition widely used for PSC fabrication. Solution processes are often hindered by surface tension and viscosity effects, which limit infiltration into nanoscale features and lead to non-uniform film formation^[73–75]. Whereas ALD employs gaseous precursors, enabling highly conformal coverage. Nattoo *et al.* carried out a comparative study of molybdenum disulfide (MoS_2) thin films prepared by low-temperature ALD and radio frequency (RF) sputtering focusing on their optical, structural, surface, and electronic properties^[76]. Raman spectroscopy showed that sputtered MoS_2 has weaker and broader Raman peaks, which indicates a higher concentration of defects, while the ALD films exhibited sharper features consistent with enhanced crystallinity. Transmission electron microscopy (TEM) further supported this distinction: the ALD films maintained a relatively uniform structure consisting of three to four layers, whereas the sputtered films displayed noticeable nonuniformity with amorphous MoO_x appearing at the substrate interface. Additional findings such as reduced surface roughness, higher current density, and improved mobility in the ALD samples confirmed that the ALD process is more suitable for achieving high-quality MoS_2 thin films. This capability is particularly advantageous for depositing MOs, which are essential components in PSCs and other electronic devices due to their unique properties, tunable structures, and versatile functionality^[77]. Importantly, the bandgap, composition, and nanostructure of ALD MOs can be precisely tailored to meet diverse device requirements^[78–80]. The chemisorption of MO precursors in ALD typically proceeds via ligand-exchange reactions with surface groups. For instance, in the deposition of tin oxide (SnO_2), tetrakis(dimethylamino)tin(IV) (TDMASn) as a Sn precursor reacts with surface hydroxyl groups ($-\text{OH}$), resulting in the adsorption of Sn and the release of volatile dimethylamine^[81]. Once surface saturation is achieved, the chamber is purged and H_2O is introduced as an oxidizing agent. The H_2O reacts with the

surface-bound ligands, forming Sn-O bonds while simultaneously regenerating -OH, thereby preparing the substrate for the next cycle^[82].

A key limitation of thermal ALD is its requirement for elevated temperatures to activate the self-limiting reactions, which restricts its application on thermally sensitive substrates^[83]. Plasma-enhanced ALD (PEALD) has been developed to address this issue by generating highly reactive radicals that drive surface reactions at low temperature^[84,85]. This reduces thermal damage, making the process suitable for organic layers and completed devices, including flexible PVs^[86,87]. However, the lower processing temperatures of PEALD can compromise precursor reactivity, often leading to the incorporation of carbon and nitrogen impurities and the formation of amorphous or polycrystalline films with reduced electrical conductivity^[88]. Optimizing PEALD parameters including process temperature, plasma conditions, and pulse times can help mitigate these limitations, as these variables strongly influence film crystallinity, impurity content, density, and uniformity. For example, Xu *et al.* systematically compared the film growth behavior, microstructural characteristics, and electrical properties of SnO₂ thin films deposited on Si wafers via thermal ALD, PEALD, and layer-by-layer Ar plasma treatment (PEALD-ALT)^[89]. All films were deposited at 250 °C using TDMASn as the Sn precursor, while O₃, O₂ plasma, and an additional Ar plasma step were employed as oxidants depending on the deposition route. All processes exhibited self-limiting growth behavior; however, due to the enhanced reaction activity of O₂ plasma, the growth per cycle (GPC) was highest for PEALD. In contrast, PEALD-ALT showed a slightly reduced GPC, attributed to partial surface etching during the subsequent Ar plasma treatment. The thermal ALD film exhibited low crystallinity, whereas the PEALD film favored SnO₂ growth along the (220) orientation. In the case of PEALD-ALT SnO₂, the dominant (221) orientation was observed, which was ascribed to enhanced surface atom mobility and subsequent surface reorientation induced by Ar plasma exposure. The PEALD-ALT SnO₂ film, with increased oxygen vacancy concentration and improved crystallinity, achieved the lowest resistivity of $1.80 \times 10^{-3} \Omega\text{-cm}$, significantly lower than that of the thermal ALD film ($15.3 \times 10^{-3} \Omega\text{-cm}$), indicating improved electrical conductivity. Nevertheless, physical ion bombardment, grain growth, densification, and local temperature rise during plasma treatment introduced substantial residual stress, leading to increased surface cracking and roughness. Overall, this approach enables the growth of highly conductive and crystalline SnO₂ films without high-temperature post-annealing, offering a promising route for fabricating transparent conductive oxides and charge-transport layers suitable for flexible or thermally sensitive optoelectronic devices.

ALD requires a long processing time because precursor pulsing and chamber purging need to be repeated for every cycle^[90,91]. As the desired film thickness increases, the required number of cycles rises proportionally, making throughput a critical challenge for large-scale production. Spatial ALD (SALD) has been introduced as a promising solution to the bottleneck. Apart from conventional ALD where precursors and purging gases are introduced sequentially within a single chamber, spatial ALD separates these steps into distinct areas^[92,93]. As the substrate continuously moves through separated zones, adsorption and purging occur in parallel, eliminating downtime between pulses and enabling high-speed deposition. This continuous process accelerates growth rates and is also compatible with roll-to-roll process, thereby facilitating scalable deposition on large-area and flexible substrates^[94]. Notably, while SALD ensures reasonable thickness control and uniformity through self-limiting reactions, it inherently necessitates complex reactor architectures, stringent gas flow regulation, and meticulous optimization of operational parameters such as substrate movement speed and gas flux, thereby elevating the overall process complexity^[95,96]. For instance, Jiang *et al.* adopted SALD to circumvent the chamber-size limitations and slow cycling speed of thermal ALD for large-area SnO₂ film growth^[97]. The process was carried out at 100 °C to ensure compatibility with perovskite layers, oxidants with different reactivities were compared using TDMASn as the tin precursor. The oxidation state and vacancy concentration were effectively regulated by varying the oxygen sources. The GPC of SnO₂ with H₂O₂ was 2.05 Å cycle⁻¹, and saturation growth was observed when the TDMASn and H₂O₂ flow rates

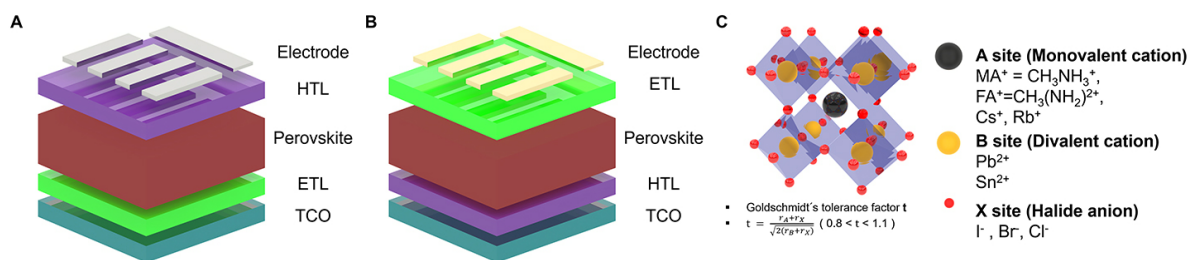


Figure 3. (A) Device structures of regular and (B) inverted PSCs. (C) Schematic illustration of halide perovskite structure.

were set to 250 and 50 sccm. Moreover, the substrate transport velocity and the nozzle-substrate spacing (micro-gap) were optimized as key process parameters. At a substrate velocity of 75 mm/s, the thickness nonuniformity across a $20 \times 20 \text{ cm}^2$ substrate was minimized to 2.24 %. When the micro-gap was increased beyond 1.0 mm, the precursors injected from adjacent channels intermingled, leading to enhanced CVD-type growth and a consequent decrease in film uniformity. The optimization of precursor type, reactivity, substrate transport, and reaction-zone width in SALD is essential to achieving uniform film thickness, smooth surface morphology, and desirable electrical properties such as high carrier mobility and low resistivity.

Despite several challenges, ALD remains one of the most precise and versatile deposition techniques available. With its ability to finely tune film properties and ensure excellent conformality, ALD encompassing both conventional and spatial approaches offers significant potential for enhancing the efficiency and stability of PSCs while simultaneously providing a scalable pathway for industrial applications and large-area device fabrication.

Configuration of PSCs

Typical PSCs are generally categorized into the two architectures, namely regular (n-i-p) and inverted (p-i-n), according to the deposition sequence of the charge transport layers (CTLs) on the transparent conducting oxide (TCO). Both structures are composed of five basic layers, which include the electrodes, CTLs, and perovskite absorber [Figure 3A and B]. Upon illumination, the perovskite layer generates charge carriers, which are separated and transported through the respective CTLs to be collected at the electrodes. Halide perovskites are crystalline materials with the formula ABX_3 , where the A site is occupied by a monovalent organic or inorganic cation, the B site by a divalent cation such as Pb^{2+} or Sn^{2+} , and the X site by a halide anion^[98,99] [Figure 3C]. Calculated from the ionic radii of the constituent ions, the Goldschmidt tolerance factor (t) serves as an indicator of perovskite structural stability. A value near ~ 1 suggests the formation of an ideal cubic phase^[100]. The framework of corner-sharing $[\text{BX}_6]$ octahedra provides pathways for charge carriers generated by light absorption^[101]. The valence band (VB) and conduction band (CB) are derived from orbital interactions between B- and X-site ions, while the A-site cation indirectly influences band structure by modifying B-X bond lengths and angles^[102]. As a result, halide perovskites exhibit a direct bandgap that facilitates efficient charge carrier generation without requiring momentum change, and their bandgap can be readily tuned by halide substitution^[103]. For example, replacing I⁻ with Cl⁻ increases the bandgap from ~ 1.5 to $\sim 2.4 \text{ eV}$ due to altered orbital overlap between halide anions and B-site cations^[104]. Similarly, replacing Pb^{2+} with Sn^{2+} enhances s-p antibonding within the octahedra, leading to a bandgap reduction^[105]. This endows halide perovskites with strong optical absorption, ambipolar charge transport, and convenient solution processability, making them attractive absorber materials for high-efficiency solar cells.

Despite their outstanding optoelectronic properties, perovskites suffer from intrinsic and environmental instabilities that limit device operation. The photoactive cubic α -phase of FAPbI_3 , which is suitable for light

harvesting is thermodynamically unstable at room temperature and tends to convert into the photoinactive hexagonal δ -phase^[106]. In addition, the soft ionic lattice results in low defect formation energies, enabling facile migration of organic cations and halide anions^[107]. This generates a high density of vacancies, interstitials, and substitutional defects, which act as nonradiative recombination centers and exacerbate ion migration. Such instabilities are further accelerated under operational conditions by exposure to light, moisture, and heat^[108]. Light and heat promote volatilization of organic cations and activate ion migration, while water molecules irreversibly hydrolyze perovskites into precursors such as organic salts and PbI_2 ^[109]. Grain boundaries and defects in perovskite films provide diffusion pathways for moisture ingress, while oxygen and illumination lower the activation energy for decomposition and perpetuate degradation cycles^[110,111].

Strategies comprising compositional engineering in which A-site cations or halide anions are mixed to stabilize the lattice together with the introduction of additives during film growth to suppress defect formation, can mitigate these issues but do not fundamentally resolve the thermodynamic instability of the material^[112,113]. As a result, interface engineering has emerged as an additional strategy to improve both efficiency and stability, through the introduction of interlayers or surface modifications at the perovskite/CTL interface^[114,115]. MOs are considered highly attractive materials because of their chemical robustness and long-term durability. They passivate interfacial defects, impede the permeation of moisture and oxygen, and suppress degradation induced by ion migration between metal electrodes and neighboring layers^[116–118]. Owing to beneficial functionalities, MOs function both as buffer layers and as encapsulation materials that shield the device from external environments^[93,119]. MOs exhibit efficient charge transport because oxygen vacancies act as electron-donating defects in n-type MOs, while metal-ion deficiencies generate holes in their p-type counterparts^[120]. Owing to their inherently high carrier mobility and tunable semiconducting behavior, MOs can also be readily engineered into diverse nanostructures. MOs are particularly attractive for low-cost, large-area fabrication, and their thin-film properties such as crystallinity, particle size, and defect concentration can be finely adjusted through process parameters including annealing temperature and atmosphere. These characteristics can be further optimized by controlling deposition temperature and pressure in a range of vapor-phase deposition methods.

In PSCs, CTLs are typically constructed from either organic materials or MOs. Common electron transport layer (ETL) materials include fullerene (C_{60}) and derivatives such as phenyl-C61-butyric acid methyl ester (PCBM), as well as n-type MOs such as TiO_2 , SnO_2 , and zinc oxide (ZnO)^[121,122]. For hole transport layers (HTLs), conductive polymers such as poly(3,4-ethylenedioxythiophene):poly(styrenesulfonate) (PEDOT:PSS), small molecules like 2,2',7,7'-tetrakis(N,N-di-p-methoxyphenyl-amine)9,9'-spirobifluorene (spiro-OMeTAD), and p-type MOs such as nickel oxide (NiO) are widely employed^[123–125]. Although TiO_2 exhibits excellent optical properties and chemical stability, its low conductivity limits its applicability as an efficient charge-transport layer in PSCs^[126]. SnO_2 , by contrast, provides high electrical conductivity and strong adhesion to flexible polymer substrates, which helps prevent delamination and cracking and thereby enhances mechanical reliability^[127]. Both MOs exhibit outstanding chemical stability and high electron mobility, making them suitable as electron-transport and buffer layers in solar cells and ferroelectric devices. ZnO allows wide tunability of n-type conductivity and resistivity through doping and defect engineering, and it can be synthesized in various nanostructures^[128]. The strong piezoelectric properties further enable applications in energy harvesting, sensing, and other electronic devices. The appropriate materials designated for CTLs need to exhibit appropriate energy-level alignment, high conductivity, and sufficient carrier mobility, with the specific selection depending on whether the device is fabricated in the regular or inverted configuration. In regular devices, the ETL is deposited directly on the TCO and can therefore tolerate high-temperature processing. Typically MOs require temperatures above 150 °C, and NiO can also be employed under similar high-temperature conditions in HTL of inverted structure^[129]. MOs are

advantageous due to their chemical and thermal stability, energy-level compatibility with perovskites, and ability to be fabricated via simple spin-coating process^[130]. However, the requirement for high-temperature annealing and the limited solvent choices restrict their application as regular HTLs, inverted ETLs, or in flexible device. Organic CTLs can be deposited at low temperatures, making them more compatible with perovskite layers and polymeric substrates^[131]. For instance, spiro-OMeTAD commonly used as an HTL in regular structures is formed without any annealing and offers favorable energy-level alignment with perovskite absorbers^[132]. In inverted structures, HTLs must be stable against both high-temperature annealing (≥ 100 °C) and polar solvents such as dimethylformamide (DMF), making PEDOT:PSS, PTAA, and carbazole-based self-assembled monolayers (SAMs) such as [2-(9H-carbazol-9-yl)ethyl]phosphonic acid (2PACz) suitable options^[133].

Nevertheless, organic CTLs face limitations including high cost due to complex synthesis and purification, the need for additional dopants to improve charge transport, and poor stability under operational conditions. Spiro-OMeTAD requires Bis(trifluoromethane)sulfonimide lithium and cobalt salts (Li-TFSI, Co-TFSI) to compensate for low hole mobility, yet these metal ions can migrate into perovskite vacancies and impair stability^[134]. Fullerene-based ETLs also suffer from limited tunability of energy levels and poor photostability^[135].

With the aim of mitigating the issues, inorganic MOs with superior intrinsic properties can be deposited directly onto perovskite layers or flexible substrates by ALD. ALD MO layers exhibit low pinhole density, high compactness, and effective barrier properties against moisture and oxygen, thereby improving both efficiency and stability^[136]. Moreover, ALD layers can function not only as standalone CTLs but also as bilayer structures in combination with solution-processed CTLs, as interfacial or buffer layers between the perovskite and CTLs, or between CTLs and electrodes^[77,137]. Al_2O_3 with insulating nature from wide bandgap hardly serve as an electron transport material but can act as a hole-blocking and defect-passivating interlayer. Owing to chemical and thermal stability, it can also be applied as a thin buffer layer or in encapsulation to enhance device lifetime. Despite their chemical stability, metal top electrodes are prone to degradation through the formation of metal halides driven by ion migration under illumination^[138]. The insertion of ALD MO buffer layers between HTLs and metal electrodes suppresses such reactions and improves thermal stability^[139]. Encapsulation processes incorporating MOs also play a crucial role in preventing direct exposure of perovskites to moisture and oxygen. While organic encapsulants such as ethylene vinyl acetate (EVA), poly(ethylene terephthalate) (PET), and epoxy resins are mechanically flexible and compatible with low-temperature processing, they provide insufficient barrier performance compared to inorganic oxides^[140,141]. ALD MOs fabricated at low temperature thus presents an effective solution for encapsulation, offering superior moisture and oxygen impermeability without compromising device integrity^[142]. Indeed, the insufficient stability of perovskite absorbers necessitate the incorporation of additional interfacial and barrier layers within PSC architectures. ALD MOs with defect passivation capability, robust stability, and barrier properties represent a particularly effective strategy to simultaneously enhance the efficiency, durability, and scalability of perovskite solar cells.

APPLICATION OF ALD MO IN PSC

The efficiency and stability of PSCs are strongly dependent on the optoelectronic, physical, and chemical properties of the constituent layers. Over the past several years, approaches informed by fundamental insights into perovskite degradation mechanisms and charge carrier dynamics have led to significant improvements in device efficiency^[143]. Nevertheless, the intrinsic instability of perovskite materials arising from their weak ionic bonding remains a major challenge, particularly with respect to vulnerability against external factors such as moisture and oxygen^[144]. In addition to improving the crystallinity of the perovskite absorber itself, interfacial modification through the incorporation of interlayers and the introduction of

encapsulation strategies have been proposed as effective means to enhance device stability^[42]. Accordingly, the materials used in layers of PSC should provide excellent chemical and physical stability, control interfacial defects without hindering light absorption or charge transport, and offer long-term durability. MOs with high environmental resistance represent highly promising candidates for device fabrication. The valence band maximum (VBM) of MO is typically derived from O 2p orbitals, while the conduction band minimum (CBM) arises from the outer orbitals of metal cations^[145]. The resulting large energy separation generally renders them wide-bandgap semiconductors. Since the bonding characteristics, crystal structures, and oxidation states vary depending on the metal cation, appropriate MOs can be selected for each functional layer of PSCs. For instance, SnO₂, TiO₂, and NiO are semiconductors whose energy levels align well with perovskite absorbers, allowing efficient electron or hole extraction and transport^[146]. In contrast, Al₂O₃ with a bandgap exceeding 7.0 eV is an insulator unsuitable for CTLs but highly chemically stable, thus serving effectively as a barrier against unwanted penetration of external species^[147]. Solution-based deposition of MOs, however, often requires high-temperature annealing for crystallization, introducing defects and impurities^[148]. The ALD MOs provide uniform and conformal films with atomic-scale thickness control, offering a promising approach to overcome the limitations. This section will examine the roles of ALD MO layers in PSCs and the specific characteristics of the associated processes.

ALD MO layer deposition for TCO electrodes

The front contact of PSC should maximize light transmission to the perovskite absorber while simultaneously ensuring proper energy-level alignment with CTLs. TCOs are employed as their wide bandgap provides optical transparency without hindering light absorption, while doping with elements such as Sn or fluorine (F) confers high electrical conductivity^[149,150]. TCOs also offer excellent chemical stability and durability, making them compatible with high-temperature processing. Among single-junction PSCs, indium tin oxide (ITO) and fluorine-doped tin oxide (FTO) are the most commonly used transparent electrodes^[151]. The transparent films can be prepared through various techniques including spray pyrolysis, TE, and CVD, with magnetron sputtering-produced ITO-coated glass serving as a representative large-area substrate^[152]. Although these processes ensure reasonable reproducibility, uniformity, and deposition speed, the utilization of ALD confers exceptional control of surface chemical properties. The surface of conventional ITO typically contains hydroxyl groups bound through both physical adsorption and chemisorption^[153]. However, when the OH group forming weak hydrogen bonds is lost during the processes, the functional group of the SAM-based HTLs fails to anchor to the surface of substrate, resulting in reduced coverage^[154]. To address this, Tang *et al.* introduced ITO films modified by ALD using TDMASn and trimethylindium precursors to prevent the desorption of OH groups caused by strong polar solvents^[155]. The resulting ALD ITO fabricated by alternating cycles of In₂O₃ and SnO₂ deposition preserved a high density of covalently bound hydroxyl groups even after DMF treatment. MeO-2PACz and (3,6-dimethoxy-9H-carbazol-9-yl)trimethoxyphenylsilane (DC-TMPS) as SAM HTL were subsequently immobilized on the ALD ITO surface. While MeO-2PACz features a bidentate phosphonic acid anchoring group, DC-TMPS incorporates a tridentate trimethoxysilane group, which forms stronger bonds with surface hydroxyls. As a result, both molecules improved the power conversion efficiency (PCE) of PSCs fabricated on ALD ITO substrates, but DC-TMPS in particular yielded superior enhancements in light and thermal stability. In contrast to ITO, which relies on the expensive and scarce element indium, aluminum-doped zinc oxide (AZO) is composed of abundant, nontoxic elements (Zn and Al), making it a low-cost alternative^[156-158]. de Melo Monteiro Modesto *et al.* reported ALD-grown AZO films using diethylzinc (DEZ) and trimethylaluminum (TMA) as Zn and Al precursors^[159]. The resulting AZO exhibited over 80% transmittance in the visible region, a bandgap greater than 3.3 eV, and a low resistivity of $1.26 \times 10^{-2} \Omega\cdot\text{cm}$, indicating its potential as an effective TCO layer for enhancing light absorption and charge transport in PSCs. Despite these promising results, however, the electrical conductivity and optical transmittance of AZO remain inferior to those of ITO and FTO, underscoring the need for further optimization.

ALD MO layer deposition for CTLs

MOs for ETL

The ETL in PSCs is expected to be capable of electron extraction and hole blocking, in addition to offering high electron mobility, optical transmittance, facile and uniform film formation, and chemical stability. On account of the demanding requirements, the materials employed as ETLs have been selectively chosen depending on the device architecture. In regular type PSCs, the ETL is fabricated prior to the perovskite layer, and therefore high-temperature annealing can be employed. Although this limits the use of flexible substrates, MO-based ETLs such as SnO_2 and TiO_2 fabricated through high-temperature processing fulfill most of the required conditions. More recently, advances in sol-gel precursor design and quantum dot (QD) solution processing have facilitated the low-temperature ($< 150^\circ\text{C}$) formation of MO ETL, yet film non-uniformity and surface/bulk defects continue to persist^[160,161].

As a process to improve the quality of ETLs, ALD can provide highly pure and conformal thin films without defects and offers precise control at the atomic scale as well as the ability to modify chemical properties through doping or precursor adjustment, being applied either alone or in combination with solution processes. Hsu *et al.* fabricated tantalum (Ta)-doped TiO_2 films to improve the conduction-band mismatch and high resistivity of TiO_2 ETL^[162]. By simultaneously introducing titanium isopropoxide (TTIP) and tantalum ethoxide ($\text{Ta}(\text{OEt})_5$) precursors and controlling the Ta concentration by adjusting the bubbler temperature in the range of $70\text{--}90^\circ\text{C}$, Ta-doped TiO_2 films were deposited through PEALD. This process induced the formation of oxygen vacancies, reduced the bandgap from 3.17 to 3.0 eV, and shifted the conduction band downward, thereby decreasing the resistivity to the level of $10^{-1}\ \Omega\cdot\text{cm}$. XPS results confirmed the reduction of Ti^{4+} to Ti^{3+} and Ti^{2+} , accompanied by oxygen vacancies acting as donor levels, which increased the free electron concentration [Figure 4A]. Devices based on the improved ETL exhibited a PCE increase from 13.4% to 18.1%, while the hysteresis index (HI) decreased from 1.06% to 0.21%. When excessive Ta doping was introduced due to overly high bubbler temperatures, defect formation increased and efficiency decreased. Chai *et al.* introduced ALD TiO_2 to overcome difficulties in completely covering the rough FTO substrate with solution-processed TiO_2 ETL^[163]. The ALD TiO_2 fully covered the protrusions of the FTO surface, suppressing leakage current. The solution-processed TiO_2 deposited on top elevated the CBM, forming better energy-level alignment with the perovskite layer [Figure 4B]. Steady-state PL (ssPL) spectra showed that the PL peaks of CsPbI_3 deposited on TiO_2 bilayers were blue-shifted, confirming improved crystallinity [Figure 4C]. As a result, the device incorporating ALD TiO_2 exhibited enhanced electron transport, increasing the PCE from 18.80% to 19.60% and maintaining stable output under operational conditions. Nb-doped TiO_2 ETLs were fabricated by adjusting the ratio of Ti and Nb sources, where the incorporation of Nb atoms into the TiO_2 lattice caused lattice expansion^[164]. Through a supercycle ALD process with TTIP, tris(diethylamido)(tert-butylimido)niobium(V) (TBTDEN), and H_2O precursors, the Nb incorporation was controlled. The sequence of $\text{Ti-H}_2\text{O-Nb-H}_2\text{O}$ proved to achieve the most stable Nb doping. The deposited films were controlled to a thickness of 15 nm, and upon annealing at 500°C , the anatase crystalline phase was formed, improving the electronic structure and optical properties. With increasing Nb content in the ALD TiO_2 , J_{sc} , V_{oc} , and FF improved, and under optimized conditions, the PCE reached 18.3%, surpassing that of pristine TiO_2 (16.2%) and Nb_2O_5 (16.45%). In stability assessments, the devices retained $\sim 17.6\%$ efficiency after 61 days of shelf aging and maintained 80% of their initial performance after 138 h under continuous illumination under ISOS-L1 conditions. In conclusion, the doping concentration in TiO_2 ETLs must be precisely controlled, and ALD demonstrates its effectiveness in achieving such fine-tuned optimization.

SnO_2 generally exhibits higher electron mobility than TiO_2 and provides better conduction band alignment with perovskite absorbers, while also being deposited at lower temperatures^[165,166]. Due to suppressed charge recombination losses, highly efficient regular type PSCs frequently employ SnO_2 as the ETL^[167,168]. SnO_2 is

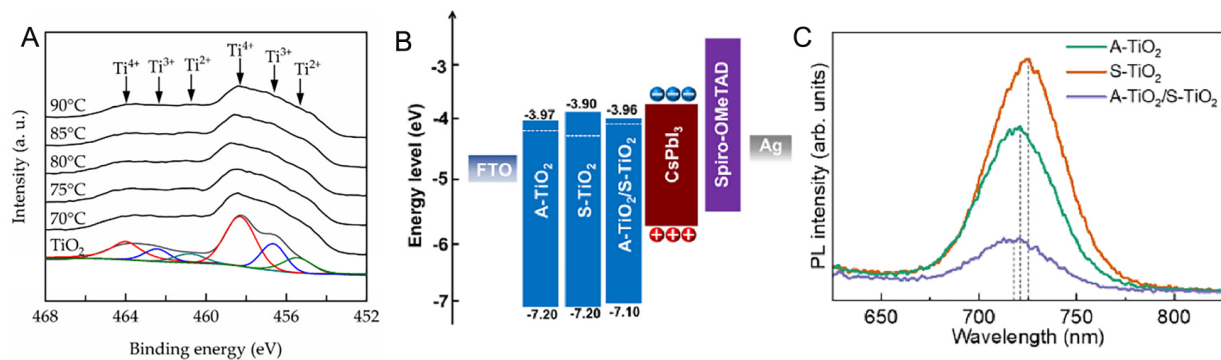


Figure 4. (A) O 1s core-level spectra from XPS analysis of Ta-doped PEALD-grown TiO_2 thin films at varying bubbler temperatures^[162]. Copyright 2021, MDPI. (B) Energy band diagram of ALD (A-)/solution (S-)/bilayer TiO_2 ETL-based devices^[163]. Copyright 2023, Elsevier. (C) ssPL spectra of A-/S-/bilayer TiO_2 film^[163]. Copyright 2023, Elsevier.

usually deposited by solution-based methods involving sol-gel, colloidal nanoparticle dispersion, and chemical bath deposition (CBD), which are cost-effective and compatible with large-area production. However, these approaches often face challenges with film uniformity and thickness control, and they readily introduce surface defects such as impurities and oxygen vacancies that act as trap sites, thereby reducing electron extraction efficiency^[169,170]. Incorporation of ALD helps overcome such issues, promoting the high-quality SnO_2 even at low temperatures through careful control of process parameters. Above a certain temperature threshold, ALD SnO_2 growth deviates from self-limiting behavior and transitions toward CVD-like deposition^[171]. Although oxygen vacancies can increase carrier density, they simultaneously reduce mobility due to enhanced scattering^[172]. Therefore, a balance of thermal energy and optimized processing conditions is required to activate surface reactions for uniform film growth while minimizing defect formation. Martinez-Puente *et al.* optimized process conditions for remote and direct plasma ALD (RPALD and DPALD) of SnO_2 using TDMASn and oxidants^[173]. When hydrogen unintentionally substituted for oxygen vacancies, it acted as a shallow donor and induced surface plasmon resonance (SPR). The hot electrons generated by SPR were injected into the SnO_2 /perovskite interface, promoting photocatalysis. However, doping was minimized under RPALD conditions at 80 °C with O_2 as the oxidant. While the growth of the ALD SnO_2 can be precisely controlled, SnO_2 often performs better when fabricated as a bilayer in combination with solution-based methods rather than solely by ALD when applied to the TCO in regular type PSCs. Gong *et al.* analyzed the challenges associated with coating ITO using ALD SnO_2 ^[174]. Interestingly, the roughness of the ALD SnO_2 film was found to be higher than that of both bare ITO and solution-processed SnO_2 , which resulted in a reduced charge transport efficiency in the device. The observed roughness increase was attributed to the inherent nature of ALD, as the repeated atomic-scale deposition process tends to amplify the pre-existing surface irregularities of the ITO. In contrast, spin-coating a solution allows the film to spread and self-level across the substrate surface. Conversely, the bilayer SnO_2 film - fabricated by subsequently depositing a solution-processed layer on top of the ALD layer - exhibited the lowest roughness. This improvement was attributed to the initial ALD layer enhancing the chemical affinity between the substrate and the solution, thereby enabling a more uniform coating. The charge extraction efficiency of the various SnO_2 coatings was further investigated using time-resolved photoluminescence (TRPL) spectroscopy on ITO/ SnO_2 /perovskite films. The TRPL results revealed that the ALD-coated film exhibited a shorter decay time compared with the spin-coated film, indicating more efficient charge transfer at the interface. Zhang *et al.* also combined with sol-gel derived SnO_2 in a bilayer suppressed colloidal aggregation, reduced surface roughness, and increased the contact angle, improving PbI_2 crystallization^[175] [Figure 5A]. Grazing-incidence wide-angle X-ray scattering (GIWAXS) confirmed superior orientation and

intensity of the bilayer-derived PbI_2 films, as indicated by (100) plane azimuthal cuts [Figure 5B and C]. TRPL measurements revealed a notable reduction in decay components. The fast decay lifetime (τ_1) corresponding to electron transfer from the perovskite to the interface decreased from 18.53 ns for the sol-gel SnO_2 film to 10.10 ns for the bilayer film. Similarly, the slower recombination component (τ_2), associated with defect-mediated recombination, declined from 71.32 to 38.12 ns. Consequently, the average carrier lifetime shortened from 60.20 to 30.61 ns. The accelerated PL decay indicates more efficient electron extraction into the ETL and reduced defect-assisted recombination. Furthermore, XPS analysis of the O 1s and Sn 3d core levels confirmed improved interface stability. The XPS spectra showed an increased $\text{Sn}^{4+}/\text{Sn}^{2+}$ ratio and a lower density of surface oxygen vacancies, evidencing enhanced film stoichiometry and reduced interfacial defects. Consequently, the champion device achieved a PCE of 23.86%, representing enhancement over the 22.09% control. Ge *et al.* introduced V-shaped nanoplate FTO (NP-FTO) substrates to mitigate energy losses from oblique light incidence and nonradiative recombination associated with conventional ITO and FTO^[176]. Integrating sphere and angle-resolved reflection (ARR) measurements showed suppressed reflectance across a wide spectral range (500–800 nm) and angles (-50° to 50°) due to the formation of a graded refractive index. Enhanced perovskite crystallization and improved carrier lifetimes were also observed. To cover the rough NP-FTO surface, SnO_2 was deposited by ALD, followed by spin-coated SnO_2 quantum dot films to form a bilayer ETL. Using TDMASn at 95 °C and H_2O at 45 °C, a 4 nm SnO_2 film was deposited over 24 cycles at 90 °C and then annealed at 150 °C for 30 min, producing a uniform, compact layer that prevented direct exposure of the substrate to the perovskite solution. This conformal ALD layer, integrated with the optically favorable NP-FTO substrate, enabled devices to reach a PCE of 26.4%, with tandem cells achieving a record efficiency of 28.2%. Chen *et al.* analyzed the influence of ALD SnO_2 on sol-gel processing, highlighting the advantages of bilayer structures^[177]. Contact angle measurements showed enhanced wettability of sol-gel solutions on ALD SnO_2 , decreasing from 37° to 21° , which facilitated smoother film growth [Figure 5D and E]. XPS analysis revealed that ALD SnO_2 exhibited a lower $\text{Sn}^{4+}/\text{Sn}^{2+}$ ratio of 1.20 compared to 1.62 in single SnO_2 , resulting in a lower refractive index (n). The reduced n value improved light transmittance, while enhanced perovskite crystallinity further minimized recombination losses, leading to a PCE of 20.55%. In stability tests under 1-sun white LED illumination in N_2 , bilayer SnO_2 retained 91.47% of its initial efficiency after 1,000 h, compared with only 71.95% for the single-layer device. Gesesse *et al.* fabricated Nb-doped SnO_2 ETLs to improve conductivity and mobility^[178]. By adjusting cycle ratios of SnO_2 and Nb_2O_5 precursors, ALD was conducted at 100 °C to control doping levels. The optimized 0.07 at.% Nb-doped SnO_2 exhibited a slightly reduced total resistance ($R_{\text{total}} = 1,961.64 \Omega\cdot\text{cm}^2$) compared with pristine SnO_2 ($2,084.88 \Omega\cdot\text{cm}^2$), enabling more efficient charge transport. However, excessive Nb content (3.45 at.%) further reduced R_{total} of $1,170.65 \Omega\cdot\text{cm}^2$ but also lowered shunt resistance (R_{sh}), resulting in higher leakage currents and a poor fill factor ($\text{FF} = 32.7\%$). Careful tuning of ALD parameters allowed optimized doping, improving PCE from 12.15% to 13.08%. Ko *et al.* proposed ultraviolet treatment to overcome the poor electrical properties and wettability of low-temperature ALD SnO_2 without requiring high-temperature annealing^[179]. Under a $400 \text{ mW}\cdot\text{cm}^{-2}$ UV source, amorphous SnO_2 transformed into nanocrystalline form as ozone and hydroxyl radicals generated from decomposed oxygen and water molecules broke unstable bonds. 10 min of UV exposure induced full crystallization, greatly improving conductivity [Figure 5F and G]. Although the process increased substrate temperature to 120 °C, limiting its applicability to flexible substrates such as ITO/PEN, the use of LED-based UV irradiation maintained the temperature at $\sim 34^\circ\text{C}$. PSCs with UV-treated SnO_2 ETLs achieved a PCE improvement from 20.36% to 22.86%, while flexible devices reached 21.49%. Lee *et al.* developed plasma-modified ALD (PMALD) SnO_x ETLs by inserting Ar plasma treatment between two Sn precursor pulses^[180]. This process precisely tuned the Sn:O ratio down to 1.38, resulting in resistivity more than four times lower and higher carrier concentrations compared to conventional ALD films. Energy-filtered photoemission electron microscopy (EF-PEEM) revealed that PMALD SnO_x exhibited a more uniform local work function (WF) distribution than nanoparticulate SnO_2 , reducing series resistance (R_s) and improving FF. Devices employing PMALD SnO_x ETLs in 23.2 cm^2 PSC

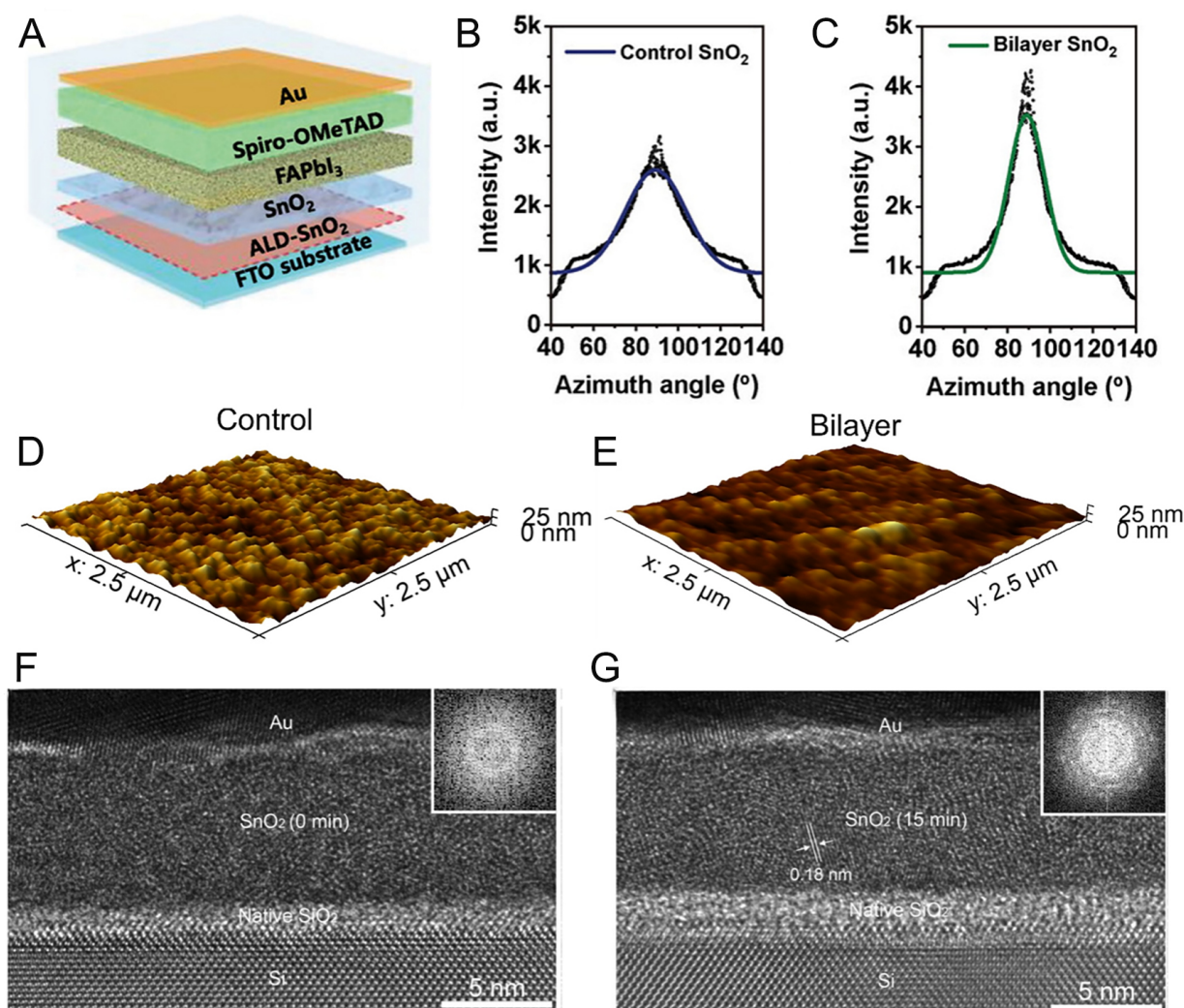


Figure 5. (A) Illustration of regular structure PSC^[175]. Copyright 2023, Wiley. (B) Azimuthal plots of solution^[175]. Copyright 2023, Wiley. (C) Azimuthal plots of ALD/solution bilayer SnO₂^[175]. Copyright 2023, Wiley. (D) 3D atomic force microscopy (AFM) surface topography images of solution^[177]. Copyright 2025, Wiley. (E) 3D AFM surface topography images of ALD/solution bilayer SnO₂^[177]. Copyright 2025, Wiley. (F) Cross-sectional TEM images of control Si/SnO₂/Au film^[179]. Copyright 2025, Wiley. (G) Cross-sectional TEM images of UV exposure after 15 min of Si/SnO₂/Au film^[179]. Copyright 2025, Wiley.

modules demonstrated a PCE improvement from 17.9% to 20.1%, while maintaining 92% of initial efficiency after 2,700 h under 85 °C and 85% relative humidity, and 96% after 1,000 h of MPPT.

ZnO is used less frequently than TiO₂ and SnO₂ despite its electron mobility and low-cost nanostructure synthesis. Its limited utilization arises from abundant Zn-related donor defects and oxygen vacancies that promote electron recombination and from strong reactivity with perovskite cations^[181,182]. Fournier *et al.* deposited compact, conformal ZnO by ALD and functionalized the surface with phosphonic acid derivatives, including 2-aminoethylphosphonic acid (2-AEPA), 4-aminobenzylphosphonic acid, and 4-fluorobenzylphosphonic acid (4-FBzPA) to address chemical instability and thermal degradation^[183]. The derivatives bonded to surface -OH groups, modifying the interface [Figure 6A]. AEPA induced uniform perovskite crystallization but restricted electron extraction due to insulating characteristics, while 4-FBzPA partially covered ZnO yet effectively suppressed degradation without hindering charge transport. These results demonstrate that ALD ZnO surfaces are able to be well-functionalized for effective interface engineering. Su *et al.* fabricated ZnO-SnO₂ bilayer ETLs by sequentially depositing ZnO and SnO₂ with

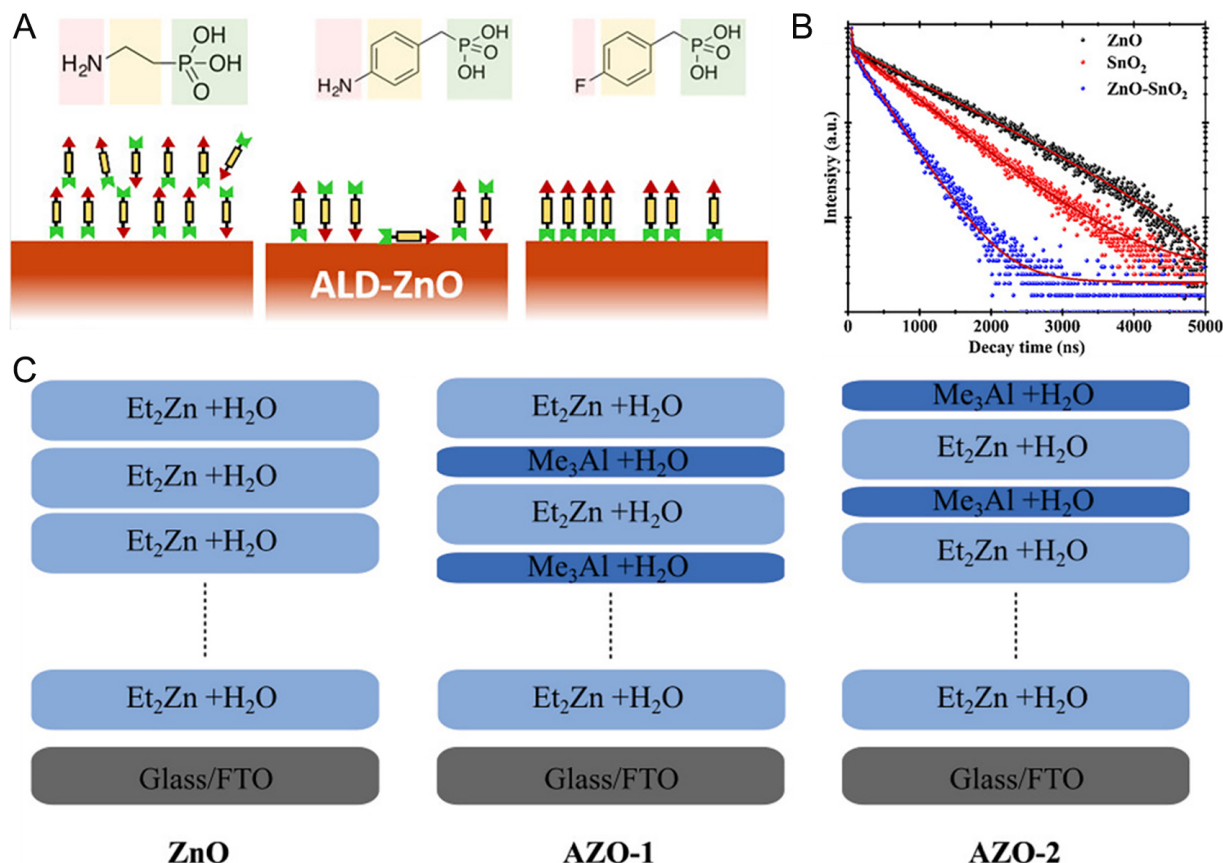


Figure 6. (A) Schematic representation of functionalized ALD ZnO surface with phosphonic acid derivatives^[183]. Copyright 2021, American Chemical Society. (B) TRPL spectra of perovskite films deposited on different ETLs^[184]. Copyright 2023, Wiley. (C) Schematic illustration of ALD processes with different terminate cycles^[157]. Copyright 2022, Wiley.

ALD^[184]. Combining the high conductivity of ZnO with the efficient electron extraction and chemical stability of SnO_2 , the bilayer exhibited reduced R_s , increased recombination resistance (R_{rec}), and faster carrier extraction as confirmed in TRPL [Figure 6B]. Wide-bandgap PSCs employing bilayers achieved $V_{\text{oc}} = 1.233$ V, $J_{\text{sc}} = 20.5$ $\text{mA}\cdot\text{cm}^{-2}$, FF = 71.6%, and PCE = 18.1% without additional surface passivation. Kruszyńska *et al.* deposited ALD AZO, optimizing stability through precursor pulsing sequences^[157]. Films fabricated with a final AlO_x pulse (AZO-2) exhibited lower resistivity, reduced band offsets, and superior thermal stability compared to those terminated with ZnO (AZO-1) due to suppression of acid-base reactions between ZnO and MAPbI_3 [Figure 6C]. Khan *et al.* investigated degradation as a function of Al concentration, finding that 5% Al doping produced perovskite films with the largest grain size and most uniform morphology^[185]. Excessively low or high concentration of Al resulted in PbI_2 formation and pinhole defects, confirmed by decreased τ_2 lifetimes in TRPL. Still, residual interfacial reactions and limited stability necessitate additional engineering.

In inverted PSCs, ETLs are deposited on top of perovskite absorbers, limiting the use of high-temperature processing. Organic ETLs such as PCBM, polyethylenimine ethoxylated (PEIE) and C_{60} are stable in polar solvents and commonly used to avoid perovskite damage but their high cost and poor stability motivate the introduction of inorganic MOs^[122,186]. Since SnO_2 can be formed at low temperatures, Rakheja *et al.* deposited ALD SnO_2 directly onto perovskite layers in inverted PSC^[187]. When deposited directly at 90 °C on FAPbI_3 or FAPbBr_3 , ALD SnO_2 induced S-shaped J-V curves. Inserting PCBM as a buffer layer between SnO_2 and perovskite mitigated the low FF. XRD confirmed the formation PbI_2 in FAPbI_3 without major structural

change, while Pb 4f_{5/2} peaks consistent with this decomposition in XPS. In FAPbBr₃, peak broadening in Br 3d and Sn 3d spectra, along with FA decomposition signals in N 1s, indicated the formation of Sn-Br bonds and decomposition pathways. These suggest that ALD SnO₂ deposition on perovskite surfaces promotes PbI₂ formation in FAPbI₃ and Sn-Br bonding in FAPbBr₃, both of which introduce electron transport barriers. The decomposition of FA cations into formamidine and triazine species during interaction with TDMASn precursors underscores the need for optimized low-temperature processes, careful precursor selection, and additional interface engineering when employing MO ETLs in inverted architectures. The performance of PSCs employing ALD-derived ETLs is summarized in Table 1.

MOs for HTL

For efficient HTL design in PSCs, materials with highest occupied molecular orbital (HOMO) levels deeper than the perovskite VBM are particularly promising as they suppress electron leakage, facilitate hole extraction, and improve stability^[194]. Prominent candidates demonstrating these features include NiO, CuO_x, CoO_x, among others^[195,196]. Notably, NiO has emerged as the most widely utilized inorganic HTL due to its favorable energy level alignment, superior stability, and compatibility with a broad range of deposition techniques represented by solution processing, vacuum evaporation, sputtering, and ALD^[197]. Inverted PSCs employing organic HTLs particularly carbazole-based SAMs have often exhibited higher efficiencies, which stems from the ability of organic molecules to precisely tune their HOMO levels relative to the perovskite VBM through molecular design, as well as the relative ease of enhancing hole mobility and conductivity via doping^[198]. Nonetheless, inorganic MOs remain attractive for commercialization, given their excellent thermal and chemical stability and cost-effectiveness. Given the presence of interfacial defects including oxygen vacancies and dangling bonds, NiO HTLs necessitate surface modification strategies, whereas ALD effectively mitigates these issues by facilitating the deposition of high-quality films.

Park *et al.* demonstrated that the instability and high cost of organic HTLs could be circumvented by employing thermally deposited ALD NiO as an inorganic HTL^[199]. Conventional ALD deposition of NiO suffers from poor reactivity, warranting plasma assistance. The nickel(II) 1-dimethylamino-2-methyl-2-butoxide [Ni(dmamb)₂] in combination with H₂O₂ or O₃ as oxidants has proven effective in producing uniform ALD NiO. XPS revealed that NiO deposited with O₃ exhibited a higher Ni-O bond ratio, ascribed to the stronger oxidizing power of O₃ compared to H₂O₂, which effectively suppressed defect formation. As a result, appropriate precursor and oxidant improved the device PCE from 18.5% to 19.7% [Figure 7A]. Phung *et al.* introduced ALD NiO films to overcome incomplete coverage of SAMs on ITO electrodes in inverted PSCs, which can lead to J_{sc} and V_{oc} reduction^[200]. The NiO layer was fabricated with bis(methylcyclopentadienyl)nickel(II) [Ni(MeCp)₂] as Ni precursor and O₂ plasma, followed by MeO-2PACz deposition without additional annealing. When both NiO and SAM were introduced onto the ITO substrate, the bilayer exhibited more uniform thickness and higher density than those obtained with either single layer. The abundant -OH groups present on the NiO surface facilitate the chemisorption and uniform growth of the SAM, which consequently gives rise to a more uniform current distribution [Figure 7B and C]. NiO as a standalone HTL exhibited low V_{oc} and fill FF due to interfacial defects, resulting in a PCE of 16.0%. In contrast, devices with SAM-covered NiO HTLs achieved an average efficiency of 19.0%, comparable to that of SAM-only systems but with improved reproducibility. Jia *et al.* developed NiO HTL using a water-based ALD without post annealing^[201]. ALD NiO typically requires strong oxidants such as O₃ or oxygen plasma in combination with high-temperature annealing, which often deteriorates interfacial stability. Bis(N,N'-di-tert-butylacetamidinato) nickel(II) (Ni(amd)₂) was employed as the precursor with H₂O oxidant for uniform NiO films enriched with -OH groups. TEM revealed that structure of ALD NiO depends on the number of ALD cycles. At 50 cycles, the film thickness was limited to ~3 nm, exhibiting diffuse diffraction patterns indicative of short-range order and amorphous-like characteristics. In contrast, 100 cycles produced a 9-10 nm film with clear diffraction spots corresponding to the cubic phase, where a lattice

Table 1. Device performance of PSCs based on ALD MO ETIs

Device structure	Product	Precursors	Thickness (nm)	GPC (Å cycle ⁻¹)	Temperature (°C)	PCE (%)	Stability	Ref.
(Regular) FTO/ALD TiO ₂ /Cs _{0.1} (FA _{0.83} MA _{0.17}) _{0.9} Pb(I _{0.83} Br _{0.17}) ₃ /spiro-OMeTAD/Au	TiO ₂	TTIP, Ta(OEt) ₅ /O ₂ plasma	60	0.284	250	18.09	-	[162]
(Regular) FTO/ALD TiO ₂ /solution TiO ₂ /CsPbI ₃ /spiro-OMeTAD/Ag	TiO ₂	TDMATi	-	-	-	19.60	AM 1.5G, RH:30% T _{86.8} = 17 h	[163]
(Regular) FTO/ALD TiO ₂ /mesoporous TiO ₂ /Cs _{0.05} (MA _{0.167} FA _{0.833}) _{0.95} /Pb(I _{0.842} Br _{0.158}) ₃ /PTAA/Au	TiO ₂	TTIP, TBTDEN, H ₂ O	15	-	200	18.3	AM 1.5G, N ₂ T ₅₅ = 138 h	[164]
(Regular) FTO/ALD TiO ₂ /MAPbI ₃ /spiro-OMeTAD/Ag	TiO ₂	TDMATi, H ₂ O	15	0.5	-	18.2	Dark, RH < 18% T ₉₀ > 336 h	[188]
(Regular) ITO/ALD TiO ₂ /MAPbI ₃ /spiro-OMeTAD/WO ₃ /Ag	TiO ₂	TTIP, H ₂ O/O ₃	80	0.9	200	-10	-	[189]
(Regular) FTO/ALD SnO ₂ /(FAPbI ₃) _{0.78} (MAPbBr ₃) _{0.14} (CsPbI ₃) _{0.08} /spiro-OMeTAD/Au	SnO ₂	TDMA Sn, H ₂ O/O ₂ /O ₃	10	1.15-1.32	80	15.15	-	[173]
(Regular) FTO/ALD SnO ₂ /solution SnO ₂ /FAPbI ₃ /spiro-OMeTAD/Au	SnO ₂	TDMA Sn, H ₂ O	5	-0.63	110	23.86	Dark, N ₂ , RH = 20% T ₈₅ = 1,300 h	[175]
(Regular) NP-FTO/ALD SnO ₂ /solution SnO ₂ /FAPbI ₃ /spiro-OMeTAD/Au	SnO ₂	TDMA Sn, H ₂ O	4	-1.66	90	25.9	AM 1.5G, 55 °C, N ₂ T ₉₅ = 1,200 h	[176]
(Regular) ITO/ALD SnO ₂ /solution SnO ₂ /MAO _{0.10} Cs _{0.05} FA _{0.85} Pb(I _{0.78} Br _{0.21}) ₃ /spiro-OMeTAD/Au	SnO ₂	TDMA Sn, H ₂ O	3.8	-1.52	120	20.22	AM 1.5G, N ₂ T _{91.47} = 1,000 h	[177]
(Regular) FTO/ALD SnO ₂ /Cs _{0.05} (MA _{0.166} FA _{0.833}) _{0.95} Pb(Br _{0.166} I _{0.833}) ₃ /PTAA/Au	SnO ₂	TDMA Sn, TBTDENM, H ₂ O	15	-	100	13.08	-	[178]
(Regular) FTO/ALD SnO ₂ /(MAPbI ₃) _{0.95} (FAPbI ₃) _{0.05} /spiro-OMeTAD/Au	SnO ₂	TDMA Sn, H ₂ O	10	0.63	125	22.86	AM 1.5G, RH = 5% T _{87.4} = 1,000 h	[179]
(Regular) ITO/ALD SnO ₂ /(FAPbI ₃) _{0.95} (MAPbBr ₃) _{0.05} /PTAA/Au	SnO ₂	TDMA Sn, H ₂ O/Ar plasma	10	-	< 200	21.8	AM 1.5G, 85 °C, RH = 85 % T ₉₆ = 1,000h	[180]
(Regular) FTO/ALD SnO ₂ /PCBM/MAPbI ₃ /spiro-OMeTAD/Au	SnO ₂	TDMA Sn, H ₂ O	-	-	120	19.3	AM 1.5G, RH = 30% T ₈₀ > 100 h	[190]
(Regular) ITO/ALD SnO ₂ /FAMAPb(I ₃) ₃ /spiro-OMeTAD/Ag	SnO ₂	TDMA Sn, O ₃	15	0.8-0.9 @ 100-150 °C 1.7 @ 250 °C	200	15.0	-	[191]
(Regular) ITO/solution SnO ₂ /ALD SnO ₂ /FAPbI ₃ /spiro-OMeTAD/Au	SnO ₂	TDMA Sn, H ₂ O	-	-	180	22.12	Dark, RH < 10% T ₁₀₀ = 240 h	[174]
(Inverted) ITO/Me-4PACz/FAPbI ₃ /ALD SnO ₂ /Ag	SnO ₂	TDMA Sn, H ₂ O	30-35	1.24	90	-	-	[187]
(Inverted) FTO/NiO/2PACz/Cs _{0.1} MA _{0.02} FA _{0.88} Pb(I _{0.98} Br _{0.02}) ₃ /ethenyltriethyloxysilane/solution SnO ₂ /ALD SnO ₂ /Au	SnO ₂	TDMA Sn, H ₂ O	40	1	100	23.0	Dark, 85 °C, RH = 10% T ₈₂ = 1,000 h	[192]

(Regular) FTO/ALD ZnO/FbzPA/Cs _{0.05} (FA _{0.83} MA _{0.17}) _{0.95} Pb(I _{0.83} Br _{0.17}) ₃ /spiro-OMeTAD/Au	ZnO	DEZ, H ₂ O	10-15	-	150	4.1	-	[183]
(Regular) FTO/ALD ZnO/ALD SnO ₂ /Cs _{0.05} FA _{0.8} MA _{0.15} Pb(I _{0.75} Br _{0.25}) ₃ /spiro-OMeTAD/Au	ZnO, SnO ₂	DEZ, TDMA Sn, H ₂ O	ZnO:28 SnO ₂ :17	-	120	18.1	-	[184]
(Regular) FTO/AZO/MAPbI ₃ /spiro-OMeTAD/Au	AZO	DEZ, TMA, H ₂ O	20	-	200	18.09	-	[157]
(Regular) ITO/In ₂ O ₃ /	In ₂ O ₃	Trimethylindium, O ₃	30	0.88	250	10.97	-	[193]

spacing of 0.21 nm was assigned to the (200) plane. Some crystallites extended through the entire film, potentially providing favorable charge transport pathways. This is consistent with the intrinsic growth mechanism of ALD, wherein ultrathin films remain stabilized in an amorphous state due to dominant surface energy, while crystallization is promoted once the critical thickness is exceeded. XPS further demonstrated that ALD-grown NiO preserved the concentration of Ni³⁺ while reducing the fraction of Ni⁴⁺, thereby suppressing undesirable interfacial oxidation reactions. The O 1s spectra revealed an enhanced fraction of -OH groups compared to ITO, and these groups were retained even after polar solvent rinsing, indicating strong chemical bonding. The abundant -OH functionalities facilitated stable adsorption of SAM molecules, resulting in improved molecular retention after cleaning. Consequently, the ALD NiO films effectively suppressed the formation of detrimental oxidized species while promoting robust SAM formation and improved interfacial quality. These collectively enhanced SAM ordering and improved the crystallinity of the subsequently deposited perovskite layer, leading to suppressed nonradiative recombination at the HTL/perovskite interface. Focusing on the surface hydroxylation of the NiO layer, He *et al.* inserted an ALD NiO buffer layer to strengthen the bonding between spin-coated NiO and Me-4PACz^[202]. The ALD buffer also enabled the formation of a denser and more uniform spin-coated NiO layer [Figure 7D]. In addition, the contact angle increased after SAM coating, indicating that Me-4PACz molecules were more densely packed. Surface potential measurements using a Kelvin probe force microscope (KPFM) revealed that hydroxylation was induced as the potential increased from -381 to -52 mV. The KPFM results are consistent with Fourier transform infrared spectroscopy (FTIR), which confirmed the formation of covalently bonded -OH groups indicated by the characteristic peak of the β-Ni(OH)_x phase. The smooth surface was particularly preferred for the interlayer, as it allows for more effective defect passivation and improved energy level alignment. Xu *et al.* incorporated [[5H-diindolo[3,2-a:3',2'-c]carbazole-5,10,15-triyl]tris(propene-3,1-diyl)]tris(phosphonic acid) (3PATAT) onto ALD NiO layers^[203]. 3PATAT introduced Ni-P bonds with the surface because of anchoring groups, suppressing undesirable reactions between Ni³⁺ species and iodide ions that would otherwise lead to PbI₂ formation [Figure 7E-G]. Furthermore, the phosphonic acid moieties strongly bonded to the ALD NiO surface while simultaneously exposing multiple hydrophilic groups, which enhanced surface wettability and facilitated improved perovskite film growth. The inverted PSC that concurrently incorporated an ALD HTL and a molecular bridging layer to achieve both thermal and moisture stability and improved perovskite film quality retained 92% of its efficiency after 1,000 h in ambient air and 80% after 500 h at 85 °C under unencapsulated conditions. In addition to the intrinsic electrical conductivity and stability of the material, NiO is advantageous for SAM deposition and interfacial engineering. Similarly, copper oxide (CuO_x) can be conformally deposited via low-temperature ALD, affording compatibility with perovskite and polymer substrates, and can be easily converted into CuI with enhanced optical transparency and charge transport^[204,205]. However, parasitic absorption due to the narrow bandgap of CuO_x remains critical drawback that limit the utilization^[206]. The device performance of HTLs fabricated by ALD is listed in Table 2.

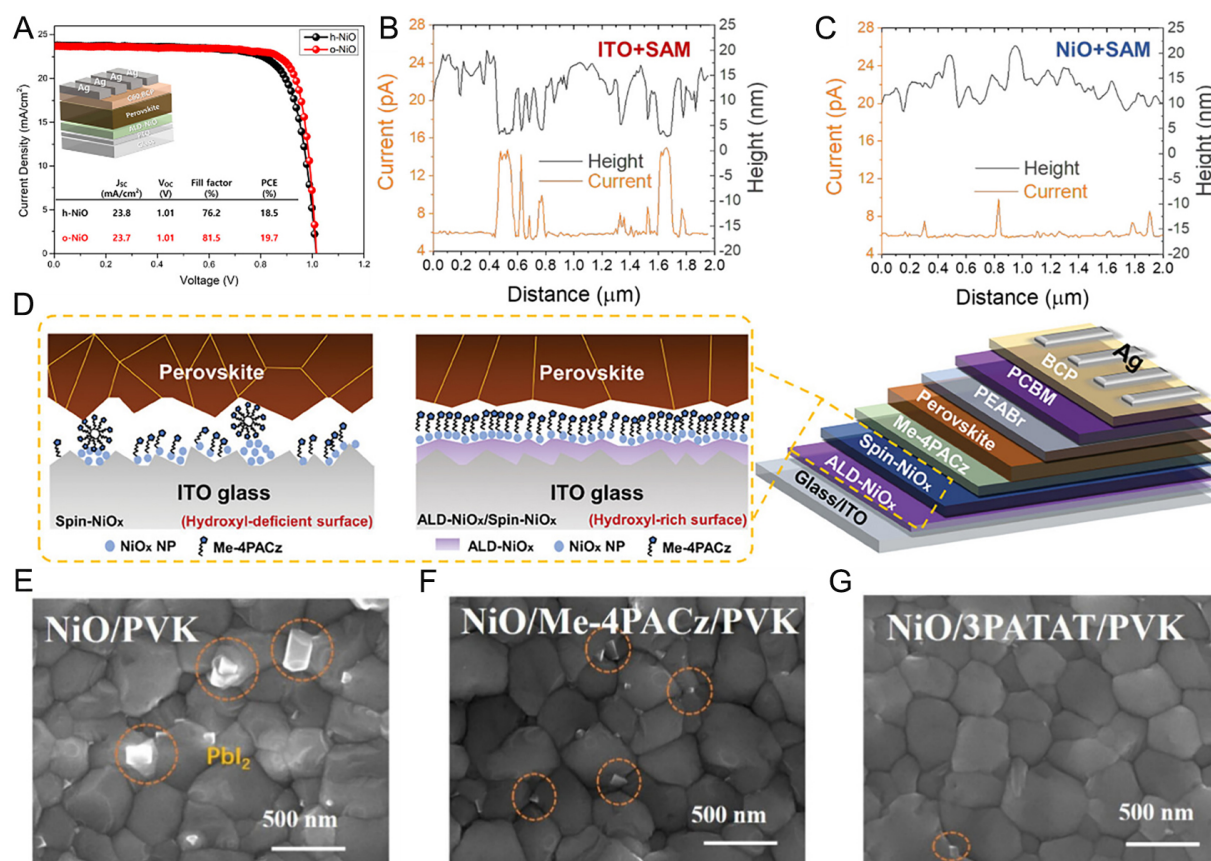


Figure 7. (A) Performance of ALD NiO based PSCs with H₂O₂(h-) and O₃(o-) oxidant^[199]. Copyright 2024, Wiley. (B) Current maps from conductive AFM line profiles of SAM and (C) ALD NiO/SAM film^[200]. Copyright 2021, American Chemical Society. (D) Illustration of the HTL/perovskite interface and the PSC structure^[202]. Copyright 2025, Wiley. (E) SEM images of perovskite films deposited on NiO (F) NiO/MeO-4PACz (G) NiO/3PATAT^[203]. Copyright 2025, American Chemical Society.

ALD MO layer deposition for interface engineering

PSCs face significant interfacial challenges as CTLs improve charge extraction and enhance performance, but interface defects at the CTL/perovskite boundary cause recombination losses^[211]. Moreover, CTLs such as spiro-OMeTAD with dopants for improving charge mobilities often exhibit hygroscopicity, accelerating device degradation^[212]. To improve both efficiency and stability, interface engineering materials are called for to simultaneously ensure effective charge transport and energy level alignment while maintaining environmental stability^[213]. Organic molecules or polymers with functional groups that mediate hydrogen bonds, ionic interactions, or Lewis acid-base coordination can stabilize undercoordinated Pb²⁺ and halide vacancies at the perovskite surface, reducing interfacial defect density, mitigating V_{oc} losses, and providing an effective passivation strategy^[214,215]. Alkylammonium halides such as phenethylammonium iodide (PEAI) and octylammonium bromide (OABr) are also widely applied. Despite their insulating nature which restricts charge transport, the organic spaces form two-dimensional (2D) perovskite more stable against moisture and oxygen than 3D phases^[216]. Nonetheless, organic molecules with optimal functionalities require rigorous density functional theory (DFT) calculations and molecular dynamics (MD) simulations for rational design. Alternatively, MOs offer a comparatively established and reliable route, with their synthesis being precisely controllable by ALD^[217]. ALD MOs with superior thermal, photochemical, and environmental stability compared to organic counterparts serve as defect-passivating interlayers and protective barriers against ion migration between electrodes and perovskites, improving long-term durability. Chavan *et al.* modified the mesoporous TiO₂ (ms-TiO₂) interface with an ultrathin ALD Nb₂O₅ layer to mitigate charge recombination^[218]. Ultraviolet photoelectron spectroscopy (UPS) and UV-vis spectra show that the CB of

Table 2. Device performance of PSCs based on ALD MO HTLs

Device structure	Product	Precursors	Thickness (nm)	GPC (\AA cycle ⁻¹)	Temperature (°C)	PCE (%)	Stability	Ref.
(Inverted) FTO/ALD NiO/Cs _{0.05} (FA _{0.95} MA _{0.05}) _{0.90} Pb(I _{0.95} Br _{0.05}) ₃ /C ₆₀ /BCP/Ag	NiO	Ni(dmamb) ₂ , O ₃	7	0.3	200	19.7	-	[199]
(Inverted) ITO/NiO/MeO-2PACz/Cs _{0.05} FA _{0.92} MA _{0.03} Pb(I _{0.83} Br _{0.17}) ₃ /C ₆₀ /BCP/Ag	NiO	Ni(MeCp) ₂ , O ₂ plasma	8	0.3	150	19.0	AM 1.5G, 85 °C, N ₂ T ₇₅ = 300 h	[200]
(Inverted) ITO/NiO/[4-(7H dibenzo[c,g]carbazol-7-yl)butyl]phosphonic Acid (4PADCB) SAM/Cs _{0.22} FA _{0.78} PbI _{2.55} Br _{0.45} /PCBM/BCP/Ag	NiO	Ni(amd) ₂ , H ₂ O	3.3	-0.66	160	23.3	AM 1.5G, N ₂ T _{84.4} = 1,000 h	[201]
(Inverted) ITO/ALD NiO/solution NiO/Me-4PACz/Cs _{0.05} MA _{0.1} FA _{0.85} PbI ₃ /phenethylammonium (PEA)Br/PCBM/BCP/Ag	NiO	Bis(cyclopentadienyl)nickel(II) (Ni(Cp) ₂), O ₃	2-3	-	250	25.25	AM 1.5G, 55 °C, N ₂ T ₈₀ = 600 h	[202]
(Inverted) FTO/ALD NiO/3PATAT/(FAPbI ₃) _{0.9} (CsPbI ₃) _{0.05} (MAPbBr ₃) _{0.05} /C ₆₀ /BCP/Ag	NiO	Ni(dmamb) ₂ , O ₃	-	-	200	25.1	Dark, RH = 20-30% T ₉₂ = 1,000 h	[203]
(Inverted) FTO/NiO/Cs _{0.05} MA _{0.95} PbI ₃ /PCBM/BCP/AZO/Ag/Al ₂ O ₃	NiO	Ni(dmamb) ₂ , O ₃	20-30	-0.25	180-230	18.8	-	[207]
(Inverted) ITO/ALD NiO/2PACz/Cs _{0.05} FA _{0.79} MA _{0.16} Pb(I _{0.75} Br _{0.25}) ₃ /C ₆₀ /ALD SnO ₂ /ITO/Ag	NiO	Ni(amd) ₂ , H ₂ O	8	-0.5	120	16.6	-	[208]
FTO/ALD NiO/(CsPbI ₃) _{0.05} ((FAPbI ₃) _{0.95} (MAPbBr ₃) _{0.05}) _{0.95} /C ₆₀ /BCP/Ag	NiO	-	~10	-	200	22.7	-	[209]
ITO/ALD NiO/Cs _{0.25} FA _{0.75} Pb(I _{0.85} Br _{0.15}) ₃ /C ₆₀ /ALD SnO ₂ /Ag	NiO	Ni(dmamb) ₂ , Cu(dmamb) ₂ , O ₃	8	-	120	22.47	0.8-sun white LED, RH = 40% T ₉₅ = 1,000 h	[210]

ms-TiO₂ lies at -3.70 eV, slightly above that of the perovskite, thus imposing a ~10 meV barrier to electron transport [Figure 8A]. A 2.1 nm Nb₂O₅ interlayer lowered the CB to -3.85 eV, resulting in more favorable electron transfer. The Nb₂O₅ also improved perovskite crystallinity, increased grain size, and smoothed the surface, as confirmed by PL, TRPL, and electrochemical impedance spectroscopy (EIS), which showed reduced nonradiative recombination, accelerated charge extraction, lower series resistance, and higher recombination resistance. Marked improvements were observed, with PCE increasing from 19.1% to 21.0%, hysteresis nearly eliminated, and long-term stability under storage, heat, and UV irradiation significantly enhanced, owing to suppression of oxygen vacancy-mediated O₂⁻ formation at the TiO₂ interface. Fabricated as an ultrathin ALD layer, Al₂O₃ reduces nonradiative recombination, blocks moisture and oxygen ingress owing to wide bandgap, optical transparency, and exceptional chemical stability. Zhao *et al.* investigated the surface chemical evolution of MAPbI₃ during Al₂O₃ ALD using in situ XPS^[219]. Upon TMA exposure, the N 1s peak shifted from 402.4 to 401.0 eV, evidencing deprotonation of CH₃NH₃⁺ to CH₃NH₂, which subsequently coordinated with undercoordinated

Pb^{2+} , effectively passivating iodine vacancies. Concurrently, CH_3I generated from the TMA-MAI reaction desorbed from the surface, suppressing iodine-related trap formation and reducing the I/Pb ratio from 4.0 to 3.6. Above 125 °C, Pb-I bond cleavage led to the formation of Pb^0 and PbI_2 . Conversely, deposition at 75 °C enabled selective Al_2O_3 growth on defect sites, reducing nonradiative recombination as τ_{avg} increased from 20.88 to 73.39 ns in TRPL results. Consequently, surface restoration and defect passivation improved the PCE from 19.2% to 20.4%, maintaining over 95% of the initial efficiency after 150 days in an N_2 -filled glove box. Yang *et al.* introduced sub-nanometer Al_2O_3 and SiO_2 layers at the NiO HTL/perovskite interface in inverted PSCs^[220]. The insulating oxides generated negative and positive fixed charges (Q_f) at Al_2O_3 and SiO_2 , adjusting carrier density distributions near the interface. Notably, the negative Q_f of Al_2O_3 attracted holes and repelled electrons, reducing recombination via an internal electric field-induced band bending. Devices incorporating a ≤ 0.5 nm Al_2O_3 layer achieved efficiency improvements from 19.8% to 22.5%, while encapsulated cells retained nearly their initial performance after 2,000 h of maximum power point tracking (MPPT) at 85 °C in ambient air. In regular PSCs, ALD Al_2O_3 deposited using TMA precursors at 60 °C suppressed moisture ingress and inhibited defect formation^[221]. DFT simulations indicated that adsorbed H_2O on layered halide perovskites react preferentially with TMA rather than A-site guanidinium(GA^+) cations, enabling deposition of ~ 3 nm Al_2O_3 films without lattice damage. The hydrophobic Al_2O_3 surface yielded devices that retained 93% of their initial efficiency after 170 h in 50% relative humidity. Choi *et al.* introduced 5-ammonium valeric acid iodide (5-AVAI) prior to ALD deposition to address film inhomogeneity arising from low-temperature oxide growth^[222]. The carboxyl groups of 5-AVAI reacted with TMA methyl groups to form Al-O bonds, facilitating uniform nucleation [Figure 8B]. Subsequent alternating TMA/ H_2O pulses produced 1.1 nm Al_2O_3 films over 10 cycles. KPFM and PL mapping revealed superior film uniformity, while TRPL showed a dramatic increase in carrier lifetime from 16.9 ns in single Al_2O_3 to 122.7 ns in 5-AVAI/ Al_2O_3 . ALD MO barrier against Ag/halide migration and moisture achieved both single-junction and tandem devices to maintain > 90% of their initial PCE after 500 h of MPPT. Ghosh *et al.* deposited Al_2O_3 directly onto completed devices to address interfacial defects introduced during spiro-OMeTAD coating in regular PSCs^[223]. PL of perovskite/spiro-OMeTAD films showed strong quenching relative to bare perovskite, with low-temperature PL at 100 K revealing a shoulder near 785 nm corresponding to defect states [Figure 8C]. During ALD, TMA precursors diffused through the HTL, reacting locally with the perovskite to form PbI_2 and passivate grain boundary defects, while H_2O oxidants remained near the surface. Devices with ALD Al_2O_3 retained > 95% of their initial efficiency after $\sim 3,200$ h of storage, compared with $\sim 60\%$ for untreated controls, and displayed superior stability under high-humidity MPPT and vacuum tests. As interfacial buffers, SnO_2 has also been adopted due to its chemical robustness, suitable band alignment, and electron transport characteristics. EVA-modified PCBM provides ester groups that bonded with TDMASn precursors, supplying additional nucleation sites for uniform SnO_2 deposition^[224] [Figure 8D]. The dense, defect-free 10 nm SnO_2 films with aligned energy levels improved FF to 79.93% and V_{oc} to 1.14 V. Similarly, Zhang *et al.* demonstrated that ultrathin (2.5 nm) ALD SnO_2 deposited at 100 °C effectively passivated defects at the C_{60} /Ag interface, overcoming incomplete BCP coverage and environmental instability^[225]. The SnO_2 buffer layers exhibited $\sim 99\%$ optical transmittance, rendering them highly suitable for tandem PSCs [Figure 8E]. In addition to Nb_2O_5 , Al_2O_3 , and SnO_2 , a wide range of oxides such as MgO , In_2O_3 , and GeO_2 have been introduced for interfacial passivation and buffer layer formation owing to their favorable optoelectronic properties and stability^[119,226,227]. Effective deployment of these materials requires precise, defect-free deposition, for which ALD serves as a central enabling technology. A summary of studies employing oxide interlayers in PSCs is presented in Table 3.

CONCLUSION

This review provides an overview of recent progress in ALD MO thin films and offers insights into their application in PSCs. ALD is particularly well-suited to the intrinsic requirements of PSCs, where both high efficiency and long-term stability are demanded. The progress of ALD allows the precise deposition of

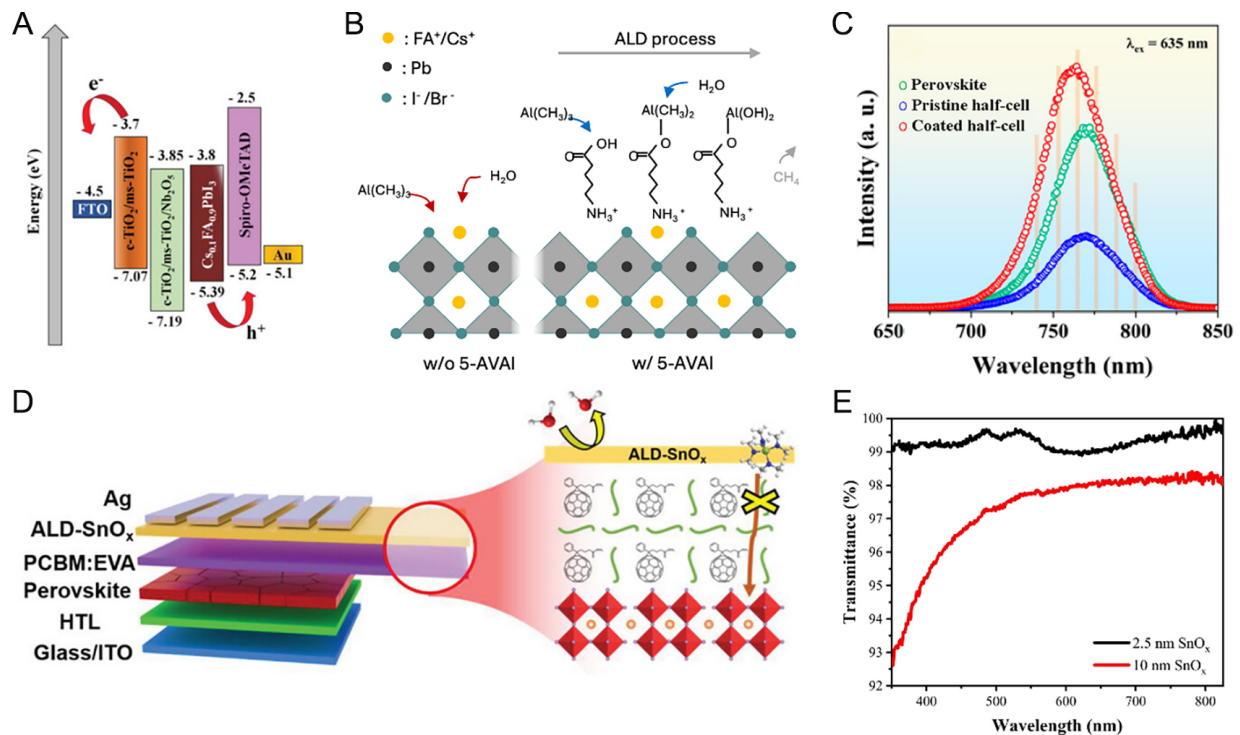


Figure 8. (A) Energy level alignment of regular type PSCs^[218]. Copyright 2021, Wiley. (B) Schematic of ALD Al_2O_3 deposition on perovskite with 5-AVAI^[222]. Copyright 2025, Elsevier. (C) ssPL spectra of perovskite film and half-cells with ALD Al_2O_3 coating^[223]. Copyright 2023, American Chemical Society. (D) Schematic illustrating passivation of perovskite/PCBM:EVA film with ALD SnO_2 ^[224]. Copyright 2023, Wiley. (E) Transmittance spectra of ALD SnO_2 films with different thickness^[225]. Copyright 2025, Elsevier.

various MOs, including SnO_2 and TiO_2 as ETLs, NiO as a HTL, and Al_2O_3 as an ion diffusion barrier, thereby providing a versatile platform for interface and structural engineering.

Through advances in process design and optimization, ALD MO layers have contributed to remarkable improvements in device performance. Building on the developments, the following subsections highlight the remaining challenges and propose future directions.

Thermal stress-induced degradation

Given that PSCs are constructed from thermally sensitive hybrid materials, the high temperatures typically required in conventional ALD represent a significant limitation. Perovskite absorbers readily decompose or suffer structural degradation above 100 °C, leading to device failure^[239]. Thermal stress decomposes the A-site organic cations, and the resulting species subsequently sublime, leaving an excess PbI_2 . The degradation becomes increasingly severe as the processing time is prolonged. In addition, elevated temperatures can thermally degrade metal precursors, compromising the self-limiting nature of ALD and leading to loss of growth-rate control, non-uniform film formation, and enhanced surface defect generation^[240]. Therefore, it is essential to develop appropriate precursors, oxidants, and processing conditions that can produce dense and conductive metal-oxide layers at low temperatures or within short deposition times. The development of precursors and oxidants that can form dense, conductive oxides at reduced temperatures is essential. However, low-temperature deposition often produces amorphous films with poor crystallinity, resulting in inferior charge transport, increased trap density, and elevated interfacial recombination^[241,242]. Although PEALD with tailored low-temperature precursor chemistry and post-deposition treatments such as

Table 3. Device performance of PSCs based on ALD MO interlayers

Device structure	Product	Precursors	Thickness (nm)	GPC (Å cycle ⁻¹)	Temperature (°C)	PCE (%)	Stability	Ref.
(Regular) FTO/TiO ₂ /ALD Nb ₂ O ₅ /Cs _{0.1} FA _{0.9} PbI ₃ /spiro-OMeTAD/Au	Nb ₂ O ₅	Nb(OEt) ₅ , H ₂ O	0.7	1.4	300	19.42	AM 1.5G, RH = 40% T ₇₆ = 700 h	[218]
(Inverted) FTO/NiO/Al ₂ O ₃ /Cs _{0.05} FA _{0.79} MA _{0.16} PbI ₃ /C ₆₀ /BCP/Cu	Al ₂ O ₃	TMA, H ₂ O	0.2-0.5	-	25	22.5	AM 1.5G, 85 °C, RH = 50% T ₁₀₀ = 2,000 h	[220]
(Regular) ITO/SnO ₂ /GA(MA) ₅ Pb ₅ I ₁₆ /spiro-OMeTAD/Ag	Al ₂ O ₃	TMA, H ₂ O	3	-1.0	60	21.0	Dark, RH = 40%-50% T ₉₃ = 4,080 h	[221]
(Inverted) ITO/NiO/Me-4PACz/Cs _{0.2} FA _{0.8} Pb(I _{0.63} Br _{0.37})/5-AVAI/ALD Al ₂ O ₃ /C ₆₀ /ALD SnO ₂ /Ag	Al ₂ O ₃	TMA, H ₂ O	1.1	1.1	100	19.5	AM 1.5G, N ₂ T ₉₉ = 615 h	[222]
(Regular) FTO/SnO ₂ /(FA _{0.83} MA _{0.17}) _{0.95} Cs _{0.05} PbI _{2.5} Br _{0.5} /spiro-OMeTAD/Au/ALD Al ₂ O ₃	Al ₂ O ₃	TMA, H ₂ O	-	-	70	20.9	AM 1.5G, RH = 60% T ₉₀ = 300 h	[223]
(Inverted) ITO/NiO/PTAA/Al ₂ O ₃ /Cs _{0.05} (FA _{0.92} MA _{0.08}) _{0.95} Pb(I _{0.92} Br _{0.08}) ₃ /PCBM:EVA/ALD SnO ₂ /Ag	SnO ₂	TDMA Sn, H ₂ O	10	-0.5	120	22.06	Dark, 85 °C, RH = 85% T ₈₅ = 800 h	[224]
(Inverted) ITO/MeO-2PACz/Cs _{0.05} FA _{0.85} MA _{0.10} Pb(I _{0.5} Br _{0.1}) ₃ /C ₆₀ /BCP/ALD SnO ₂ /Ag	SnO ₂	TDMA Sn, H ₂ O	2.5	-	100	17.90	Dark, RH = 30%-40% T _{89.6} = 552 h	[225]
(Regular) FTO/ALD SnO ₂ /solution SnO ₂ /FAPbI ₃ /spiro-OMeTAD/ALD TiO ₂ /Au	TiO ₂	TDMATi, H ₂ O	4-5	0.08-0.10	60	22.30	AM 1.5G, 0.85 V bias T _{96.5} = 120 h	[228]
(Inverted) FTO/NiO/MAPbI ₃ /Al ₂ O ₃ /PCBM/Ag	Al ₂ O ₃	TMA, H ₂ O	0.1	-0.1	75	20.4	AM 1.5G, N ₂ T _{95.3} = 3,600 h	[219]
(Regular) FTO/c-TiO ₂ /ms-TiO ₂ /FAPbI ₃ /OAI/ALD Al ₂ O ₃ /spiro-OMeTAD/Au	Al ₂ O ₃	TMA, H ₂ O	0.39	-0.10	100	23.75	AM 1.5G, 85 °C, RH = 85% T ₉₀ = 1,872	[229]
(Inverted) FTO/NiO/MeO-4PACz/(FA _{0.83} MA _{0.17}) _{0.95} Cs _{0.05} PbI ₃ /C ₆₀ /ALD Al ₂ O ₃ /Au	Al ₂ O ₃	TMA, H ₂ O	-	-	20	24.61	AM 1.5G, 65 °C, RH = 30%-50% T ₉₀ = 1,150 h	[230]
(Inverted) ITO/PTAA/Cs _{0.05} FA _{0.70} MA _{0.25} PbI _{2.25} Br _{0.75} /PCBM/AZO/ALD SnO ₂ /Ag	SnO ₂	TDMA Sn, H ₂ O	-	-	100	21.50	AM 1.5G, RH = 30%-40% T ₈₄ = 1,000 h	[231]
(Inverted) ITO/MeO-4PACz/FA _{0.7} MA _{0.15} Cs _{0.05} Pb(I _{0.83} Br _{0.17}) ₃ /C ₆₀ /ALD SnO ₂ /Ag	SnO ₂	TDMA Sn, H ₂ O	15	1.2	90	22.2	AM 1.5G, 65 °C, N ₂ T ₉₀ = 575 h	[232]
(Inverted) FTO/ALD NiO/3PATAT/Cs _{0.05} (FA _{0.95} MA _{0.05}) _{0.90} Pb(I _{0.95} Br _{0.05}) ₃ /C ₆₀ /ALD SnO ₂ /Ag	SnO ₂	TDMA Sn, H ₂ O	9-15	1.76	80-110	21.9	AM 1.5G T _{91.9} = 2,000 h	[233]
(Inverted) ITO/Me-4PACz/Cs _{0.17} FA _{0.83} Pb(I _{0.80} Br _{0.20}) ₃ /Al ₂ O ₃ /C ₆₀ /ALD SnO ₂ /Ag	SnO ₂	TDMA Sn, H ₂ O	20	1.22	80	19.26	-	[234]

(Inverted) FTO/Poly[N,N'-bis(4-butylphenyl)-N,N'-bis(phenyl)benzidine] (polyTPD)/MAPbI ₃ /PCBM/ALD SnO ₂ /PEDOT:PSS/Carbon	SnO ₂	TDMA Sn, H ₂ O	-	-	70	16.1	Real sunlight, -1-36 °C, RH = 40%-80% T ₉₄ = 500 h	[235]
(Regular) FTO/TiO ₂ /ALD HfAlO/ MAPbI ₃ /spiro-OMeTAD/Au	HfAlO	TDMAHf, TMA, H ₂ O	3	-1.0	250	9.85	AM 1.5G, RH = 40% T ₈₀ = 500 h	[236]
(Regular) ITO/SnO ₂ /(FAPbI ₃) _{0.85} (MAPbBr ₃) _{0.15} /PTAA/ALD SiAl _x O _y /ALD SiO ₂ /Au	SiAl _x O _y , SiO ₂	Tetraethyl orthosilicate (TEOS), TMAM, H ₂ O	SiAl _x O _y :5.2 SiO ₂ :7.3	SiAl _x O _y :0.52 SiO ₂ :0.24	100	19.16	Dark, RH = 85% T ₈₀ = 40 h	[237]
(Regular) ITO/SnO ₂ /Cs _{0.05} (FAPbI ₃) _{0.85} (MAPbBr ₃) _{0.15} /spiro-OMeTAD/MgO/Au	MgO	MgCp ₂ , H ₂ O	10.21	2	80	22.74	Dark, RH = 85% T ₈₀ = 162 h	[238]

passivation annealing has been investigated to address these issues, shortcomings remain due to plasma-induced substrate damage, film nonuniformity, complex parameter control, and limited large-area uniformity^[243,244]. Addressing this challenge to ensure process stability and cost-effectiveness remains critical goals.

Process and precursors compatibility

As interlayers between ETLs or HTLs and perovskite absorbers, ALD MOs facilitate selective charge transport and suppress interfacial recombination. However, strong precursor-perovskite interactions often introduce serious chemical degradation, particularly affecting the organic constituents within hybrid perovskites. Although ALD-derived SnO₂ has been widely used as a moisture-blocking protective layer for the top transparent electrodes of tandem and semitransparent PSCs, it was found to induce even faster humidity-driven degradation than bathocuproine (BCP)^[230]. During the TDMA Sn pulse step of the ALD process, the precursor triggers deprotonation of the perovskite A-site organic cations, which accelerates structural collapse under high-temperature and high-humidity conditions. Al₂O₃, owing to its strong acidic nature, suppresses these degradation pathways and improves long-term stability, yet the TMA precursor can also react with the organic cations and cause lattice disruption and defect formation^[245]. Although selecting more suitable precursors and oxidants can mitigate some of these issues, the intrinsic reactivity and thermal stability limitations of ALD restrict the process window to narrow temperature and environmental conditions required for self-limiting growth^[55,246]. When interfacial stability is insufficient, device degradation accelerates during long-term operation, with moisture and oxygen further promoting undesirable degradation pathways at the MO/perovskite interface. Consequently, precise optimization of oxide thickness, composition, deposition sequence, and interfacial treatments becomes indispensable. Although ultrathin organic buffer layers inserted prior to ALD can mitigate interfacial reactivity, chemical and structural engineering at the oxide/perovskite boundary still requires substantial refinement^[247]. A major challenge in the ALD process for PSC also lies in choosing precursors and oxide materials compatible with the chemical sensitivity of perovskites. Key precursor parameters including volatility, reactivity, stability, and byproduct generation directly determine film quality and process viability^[243]. Certain metal precursors exhibit strong reactivity with perovskites, inducing interfacial degradation or unintentional doping^[248]. For instance, TiCl₄ provides high volatility and rapid deposition kinetics but generates chlorine residues that compromise device performance^[249]. Metal-organic Ti precursors yield films of higher purity, a characteristic offset by their low volatility, which often requires elevated deposition temperatures^[250]. The structural and chemical properties of the deposited MO is determined by precursor selection, and this directly affects the electronic and optical characteristics^[251]. Accordingly, the

composition engineering of MO layers determines a decisive influence on optical transparency, electron affinity, and band alignment. Insufficient energy-level alignment of the deposited materials leads to charge transport barriers and consequently lowers efficiency^[252]. Consequently, establishing an optimal combination of precursor chemistry and oxide material is essential to balance film purity, electronic and optical functionality, and interfacial stability.

Toward commercialization

Despite the precision and controllability of ALD, the slow cycle-by-cycle growth kinetics imposes severe limitations on scalability. For PSC modules, MO films must be deposited uniformly over substrates extending to several tens of square centimeters, but the inherently low growth rate of ALD significantly limits manufacturing throughput^[253]. Moreover, when micrometer-scale MO layers are required in PV modules, the process becomes impractically time-consuming as ALD struggles to achieve even film thicknesses beyond a few tens of nanometers within reasonable durations^[254]. High equipment costs and long cycle durations further escalate production expenses. PEALD enables the deposition of MO films at low temperatures with high uniformity and smooth surfaces, making it suitable for application in PSCs. However, an excessively long precursor pulse time can induce unintended CVD reactions during the process, thereby compromising film uniformity and process controllability. Insufficient plasma exposure time, which must be carefully optimized for process throughput and efficiency, can also lead to reduced GPC, nonuniform film thickness, and degraded film quality^[255]. Highly reactive radicals cause substrate defects, complicating process control and limiting the reproducibility of low damage conditions at large scale^[256]. While SALD, roll-to-roll integration, and hybrid deposition schemes have been proposed to accelerate processes, persistent trade-offs among uniformity, throughput, and cost remain unresolved^[257,258]. In the SALD process, all precursors are introduced simultaneously into spatially separated reaction zones that are divided by physical or gaseous barriers. However, undesired gas mixing between these zones may still occur. Increasing the process temperature to accelerate reaction kinetics can lead to precursor decomposition and particle sintering, while lowering the temperature often results in incomplete adsorption and condensation of precursors^[259]. These trade-offs hinder the formation of uniform and conformal films. Therefore, although the implementation of SALD enables higher throughput and continuous operation for industrial-scale production, it inherently faces structural bottlenecks that limit film uniformity and process scalability. Achieving scalable, high-productivity ALD processes thus continues to be a major hurdle for industrial deployment.

Summary and outlook

ALD MOs represent a promising route to advancing material quality and interfacial control in PSCs. Although ALD does not yet fully surpass the simplicity and throughput of solution processing, it stands out as the most effective strategy for introducing protective buffer and encapsulation layers that enhance stability. Future progress will require the development of low-temperature precursors and processes, improved interfacial stabilization strategies, and scalable large-area manufacturing technologies. With these advancements, ALD is poised to play a decisive role in achieving both high efficiency and durability in PSCs. Ultimately, bridging the gap between academic research and industrial application through close collaboration will be pivotal in accelerating the path to commercialization of ALD. Such integrative progress is expected to drive the practical deployment of next-generation photovoltaics and contribute significantly to sustainable energy transition.

DECLARATIONS

Authors' contributions

Writing original manuscript, reviewing and editing: Park, P. J.

Reviewing and editing: Jo, H. J.; Han, S. M.; Kim, Y. J.; Kim, S. Y.

Availability of data and materials

Not applicable.

AI and AI-assisted tools statement

Not applicable.

Financial support and sponsorship

This research was supported in part by the NRF funded by the Korean government [RS-2025-00558945] and in part by Korea Institute of Marine Science & Technology Promotion (KIMST) funded by the Ministry of Oceans and Fisheries (RS-2024-00406639)

Conflicts of interest

All authors declared that there are no conflicts of interest.

Ethical approval and consent to participate

Not applicable.

Consent for publication

Not applicable.

Copyright

© The Author(s) 2026.

REFERENCES

1. Zhong, K.; Sun, P.; Xu, H. Advances in defect engineering of metal oxides for photocatalytic CO₂ reduction. *Small* **2025**, *21*, 2310677. DOI PubMed
2. Kim, J. H.; Kim, J.; Ma, J.; et al. Spontaneous metal-chelation strategy for highly dense Ni single-atom catalysts with asymmetric coordination in CO₂ electroreduction. *Small* **2025**, *21*, 2409481. DOI
3. Ma, J.; Lee, W.; Kim, J. H.; et al. Leveraging the intermetal distance in dual-atom catalysts: revealing optimized synergistic interactions for CO₂ electroreduction. *ACS. Nano*. **2025**, *19*, 18698-707. DOI
4. Oni, A. M.; Mohsin, A. S.; Rahman, M. M.; Bhuian, M. B. H. A comprehensive evaluation of solar cell technologies, associated loss mechanisms, and efficiency enhancement strategies for photovoltaic cells. *Energy. Rep.* **2024**, *11*, 3345-66. DOI
5. Jang, W. J.; Park, P. J.; Ma, J.; Kim, S. Y. Engineering perovskite solar cells for photovoltaic and photoelectrochemical systems: strategies for enhancing efficiency and stability. *Chem. Commun.* **2025**, *61*, 8137-56. DOI PubMed
6. Sabatino M, Hendawi R, Garcia AS. Silicon solar cells: trends, manufacturing challenges, and AI perspectives. *Crystals* **2024**, *14*, 167. DOI
7. Khokhar, M. Q.; Yousuf, H.; Jeong, S.; et al. A review on p-type tunnel oxide passivated contact (TOPCon) solar cell. *Trans. Electr. Electron. Mater.* **2023**, *24*, 169-77. DOI
8. Rehman, Z. U.; Lin, Z. Inorganic M₃ACl₃ (M=Ca, Sr, Ba, A=N, P, As) perovskite-derivatives for next-generation solar cells and optoelectronics: in-depth analysis of stability, optoelectronic features, and temperature-dependent carrier mobilities. *J. Mater. Chem. A*. **2025**, *13*, 34469-92. DOI
9. Wang, J.; Feng, Y.; He, Y. Advancements in recycling technologies for waste CIGS photovoltaic modules. *Nano. Energy*. **2024**, *128*, 109847. DOI
10. Camargo, P. S. S.; Petroli, P. A.; de, Souza. R. A.; et al. CdTe photovoltaic technology: an overview of waste generation, recycling, and raw material demand. *Curr. Opin. Green. Sustain. Chem.* **2024**, *47*, 100904. DOI
11. Shah, U. A.; Wang, A.; Irfan, Ullah. M.; et al. A deep dive into Cu₂ZnSnS₄ (CZTS) solar cells: a review of exploring roadblocks, breakthroughs, and shaping the future. *Small* **2024**, *20*, 2310584. DOI
12. Mahboob, S.; Rizwana, ; Kumar, G. Ozone and NaCl based electrolytic solar cell: its working principle, advantages and possibilities. *Trans. Electr. Electron. Mater.* **2021**, *22*, 536-42. DOI
13. Hedibi, A.; Gueddim, A.; Bentria, B. Numerical modeling and optimization of ZnO: Al/iZnO/ZnMgO/CZTS photovoltaic solar cell. *Trans. Electr. Electron. Mater.* **2021**, *22*, 666-72. DOI
14. Zyoud, S. H.; Zyoud, A. H.; Ahmed, N. M.; Abdelkader, A. F. Numerical modelling analysis for carrier concentration level optimization of CdTe heterojunction thin film-based solar cell with different non-toxic metal chalcogenide buffer layers replacements: using SCAPS-1D software. *Crystals* **2021**, *11*, 1454. DOI
15. Yi, J.; Zhang, G.; Yu, H.; Yan, H. Advantages, challenges and molecular design of different material types used in organic solar cells. *Nat. Rev. Mater.* **2024**, *9*, 46-62. DOI

16. Ding, P.; Yang, D.; Yang, S.; Ge, Z. Stability of organic solar cells: toward commercial applications. *Chem. Soc. Rev.* **2024**, *53*, 2350-87. DOI
17. Lee, J. W.; Park, J. S.; Jeon, H.; et al. Recent progress and prospects of dimer and multimer acceptors for efficient and stable polymer solar cells. *Chem. Soc. Rev.* **2024**, *53*, 4674-706. DOI
18. Sorrentino, R.; Kozma, E.; Luzzati, S.; Po, R. Interlayers for non-fullerene based polymer solar cells: distinctive features and challenges. *Energy. Environ. Sci.* **2021**, *14*, 180-223. DOI
19. Kojima, A.; Teshima, K.; Shirai, Y.; Miyasaka, T. Organometal halide perovskites as visible-light sensitizers for photovoltaic cells. *J. Am. Chem. Soc.* **2009**, *131*, 6050-1. DOI
20. Zhang, X.; Wu, S.; Zhang, H.; et al. Advances in inverted perovskite solar cells. *Nat. Photonics.* **2024**, *18*, 1243-53. DOI
21. Wu, T.; Qin, Z.; Wang, Y.; et al. The main progress of perovskite solar cells in 2020-2021. *Nano. Micro. Lett.* **2021**, *13*, 152. DOI PubMed PMC
22. Kothandaraman, R. K.; Jiang, Y.; Feurer, T.; et al. Near-infrared-transparent perovskite solar cells and perovskite-based tandem photovoltaics. *Small. Methods.* **2020**, *4*, 2000395. DOI
23. Wang, S.; Wang, A.; Hao, F. Toward stable lead halide perovskite solar cells: a knob on the A/X sites components. *iScience* **2022**, *25*, 103599. DOI PubMed PMC
24. Miah, M. H.; Khandaker, M. U.; Rahman, M. B.; et al. Band gap tuning of perovskite solar cells for enhancing the efficiency and stability: issues and prospects. *RSC. Adv.* **2024**, *14*, 15876-906. DOI PubMed PMC
25. Han, J.; Park, K.; Tan, S.; et al. Perovskite solar cells. *Nat. Rev. Methods. Primers.* **2025**, *5*, 3. DOI
26. Green, M. A.; Dunlop, E. D.; Yoshita, M.; et al. Solar cell efficiency tables (version 64). *Prog. Photovolt. Res. Appl.* **2024**, *32*, 425-41. DOI
27. Aydin, E.; Allen, T. G.; De, Bastiani, M.; et al. Pathways toward commercial perovskite/silicon tandem photovoltaics. *Science* **2024**, *383*, eadh3849. DOI
28. Yang, G.; Deng, C.; Li, C.; et al. Towards efficient, scalable and stable perovskite/silicon tandem solar cells. *Nat. Photonics.* **2025**, *19*, 913-24. DOI
29. Chao, L.; Niu, T.; Gao, W.; et al. Solvent engineering of the precursor solution toward large-area production of perovskite solar cells. *Adv. Mater.* **2021**, *33*, 2005410. DOI
30. Yang, F.; Jang, D.; Dong, L.; et al. Upscaling solution-processed perovskite photovoltaics. *Adv. Energy. Mater.* **2021**, *11*, 2101973. DOI
31. Wang, C.; Nie, R.; Dai, Y.; et al. Enhancing the inherent stability of perovskite solar cells through chalcogenide-halide combinations. *Energy. Environ. Sci.* **2024**, *17*, 1368-86. DOI
32. Kore, B. P.; Jamshidi, M.; Gardner, J. M. The impact of moisture on the stability and degradation of perovskites in solar cells. *Mater. Adv.* **2024**, *5*, 2200-17. DOI
33. Mesquita, I.; Andrade, L.; Mendes, A. Effect of relative humidity during the preparation of perovskite solar cells: performance and stability. *Sol. Energy.* **2020**, *199*, 474-83. DOI
34. Huang, P. C.; Yang, T. J.; Lin, C. J.; et al. Unraveling the heat- and UV-induced degradation of mixed halide perovskite thin films via surface analysis techniques. *Langmuir* **2024**, *40*, 11873-87. DOI PubMed PMC
35. Song, J.; Liu, H.; Pu, W.; et al. Thermal instability originating from the interface between organic-inorganic hybrid perovskites and oxide electron transport layers. *Energy. Environ. Sci.* **2022**, *15*, 4836-49. DOI
36. Tang, J.; Tian, W.; Zhao, C.; et al. Imaging the moisture-induced degradation process of 2D organolead halide perovskites. *ACS. Omega.* **2022**, *7*, 10365-71. DOI PubMed PMC
37. Ma, H.; Ahn, E.; Lee, D.; et al. Water-induced degradation mechanism of metal halide perovskite nanocrystals. *Matter* **2025**, *8*, 102083. DOI
38. Zhou, P.; Liu, Q.; Zhang, Z. Coupled modeling of solvent evaporation and thin film evolution in spin coating. *Appl. Therm. Eng.* **2025**, *279*, 127662. DOI
39. Sin, J.; Kim, H.; Kim, M.; et al. Anti-solvent treatment time approach to high efficiency perovskite solar cells with temperature of coating environmental. *Sol. Energy. Mater. Sol. Cells.* **2023**, *250*, 112054. DOI
40. Wang, T.; Zhang, T.; Zhang, J.; et al. Additive-regulated one-step dynamic spin-coating for fabricating high-performance perovskite solar cells under high humidity conditions. *J. Mater. Chem. C.* **2024**, *12*, 913-21. DOI
41. Al-Katrib, M.; Perrin, L.; Flandin, L.; Planes, E. Electrodeposition in perovskite solar cells: a critical review, new insights, and promising paths to future industrial applications. *Adv. Mater. Technol.* **2023**, *8*, 2300964. DOI
42. Njema, G. G.; Kibet, J. K.; Ngari, S. M. A review of interface engineering characteristics for high performance perovskite solar cells. *Measurement. Energy.* **2024**, *2*, 100005. DOI
43. Jang, W. J.; Kim, E. H.; Cho, J. H.; et al. Elucidating the role of alkali metal carbonates in impact on oxygen vacancies for efficient and stable perovskite solar cells. *Adv. Sci.* **2024**, *11*, 2406657. DOI PubMed PMC

44. Cao, Y.; Yan, N.; Wang, M.; et al. Designed additive to regulated crystallization for high performance perovskite solar cell. *Angew. Chem. Int. Ed.* **2024**, *63*, e202404401. DOI
45. Azam, M.; Ke, Z.; Luo, J.; et al. Additive engineering enabled non-radiative defect passivation with improved moisture-resistance in efficient and stable perovskite solar cells. *Chem. Eng. J.* **2024**, *483*, 149424. DOI
46. He, Z.; Peng, C.; Guo, R.; et al. High-efficiency and emission-tunable inorganic blue perovskite light-emitting diodes based on vacuum deposition. *Small* **2024**, *20*, 2305379. DOI
47. Liu, L.; Yang, S. E.; Liu, P.; Chen, Y. High-quality and full-coverage CsPbBr₃ thin films via electron beam evaporation with post-annealing treatment for all-inorganic perovskite solar cells. *Sol. Energy.* **2022**, *232*, 320-7. DOI
48. Xu, Z.; Chin, S. H.; Park, B. I.; et al. Advancing perovskite solar cell commercialization: bridging materials, vacuum deposition, and AI-assisted automation. *Next. Mater.* **2024**, *3*, 100103. DOI
49. Zhou, C.; Meng, W.; Kong, L.; et al. Vacuum processed metal halide perovskite light-emitting diodes. *Adv. Funct. Mater.* **2024**, *34*, 2307682. DOI
50. Tong, G.; Zhang, J.; Bu, T.; et al. Holistic strategies lead to enhanced efficiency and stability of hybrid chemical vapor deposition based perovskite solar cells and modules. *Adv. Energy. Mater.* **2023**, *13*, 2300153. DOI
51. Lee, J. H.; Kim, B. S.; Park, J.; et al. Opportunities and challenges for perovskite solar cells based on vacuum thermal evaporation. *Adv. Mater. Technol.* **2023**, *8*, 2200928. DOI
52. Soto-Montero, T.; Kralj, S.; Azmi, R.; et al. Single-source pulsed laser-deposited perovskite solar cells with enhanced performance via bulk and 2D passivation. *Joule* **2024**, *8*, 3412-25. DOI
53. Zhao, R.; Mao, P.; Lv, J.; et al. Atomic layer deposition processed interlayers in photovoltaics: applications, challenges and perspectives. *J. Energy. Chem.* **2025**, *109*, 702-25. DOI
54. Asare, G. K.; Adu, J. S.; Shin, B.; et al. Perspective: atomic layer deposition strategies for surface passivation of metal-halide perovskite absorbers. *Electron. Mater. Lett.* **2025**, *21*, 331-6. DOI
55. Zhang, J.; Li, Y.; Cao, K.; Chen, R. Advances in atomic layer deposition. *Nanomanuf. Metrol.* **2022**, *5*, 191-208. DOI
56. Yasmeen, S.; Ryu, S. W.; Lee, S. H.; Lee, H. B. R. Atomic layer deposition beyond thin film deposition technology. *Adv. Mater. Technol.* **2023**, *8*, 2200876. DOI
57. Tran, V. H. A.; Lims, S. C.; Anwar, N.; et al. Atomic layer deposition of metal and metal oxides: mechanisms, challenges, and future prospects. *J. Alloys. Compd.* **2025**, *1041*, 183864. DOI
58. Park, H. H.; Fermin, D. J. Recent developments in atomic layer deposition of functional overlayers in perovskite solar cells. *Nanomaterials* **2023**, *13*, 3112. DOI PubMed PMC
59. Menon, V. S.; Krishnamoorthy, A. Hole selectivity of n-type molybdenum oxide carrier selective layer for commercial and emerging thin-film photovoltaics: a critical analysis of interface energetics and ensuant device physics. *Energy. Technol.* **2023**, *11*, 2300608. DOI
60. Zhang, C.; Pei, K.; Sheng, T.; et al. Metal oxides engineering: toward sustainable superhydrophobic surfaces. *Adv. Funct. Mater.* **2025**, *36*, e12239. DOI
61. Sambathkumar, C.; Nagavenkatesh, K.; Thangavel, R.; et al. Investigation and comparative studies on charge storage performance in nanostructured RuO₂, NiO and Co₃O₄ nanoparticles for high dense energy storage. *Electron. Mater. Lett.* **2024**, *20*, 571-83. DOI
62. Singh, R.; Ghosh, S.; Subbiah, A. S.; et al. ALD Al₂O₃ on hybrid perovskite solar cells: unveiling the growth mechanism and long-term stability. *Sol. Energy. Mater. Sol. Cells.* **2020**, *205*, 110289. DOI
63. Liu, Y.; Sang, B.; Hossain, M. A.; et al. A novel passivating electron contact for high-performance silicon solar cells by ALD Al-doped TiO₂. *Sol. Energy.* **2021**, *228*, 531-9. DOI
64. Di, Mario. L.; Garcia, Romero. D.; Wang, H.; et al. Outstanding fill factor in inverted organic solar cells with SnO₂ by atomic layer deposition. *Adv. Mater.* **2024**, *36*, 2301404. DOI
65. Kim, H. M.; Kim, D. G.; Kim, Y. S.; et al. Atomic layer deposition for nanoscale oxide semiconductor thin film transistors: review and outlook. *Int. J. Extreme. Manuf.* **2023**, *5*, 012006. DOI
66. Gurbandurdyev, G.; Mistry, K.; Delumeau, L. V.; et al. Robust, conformal ZnO coatings on fabrics via atmospheric-pressure spatial atomic layer deposition with in-situ thickness control. *ChemNanoMat* **2023**, *9*, e202200498. DOI
67. Li, B.; Härtel, M.; Al-Ashouri, A.; et al. Atomic-layer-deposition-free monolithic perovskite/silicon tandem solar cell reaching 29.91% power conversion on industrial PERX/TOPCon-like silicon bottom cells. *ACS. Energy. Lett.* **2024**, *9*, 4550-6. DOI
68. Lee, S. U.; Kim, S. Y.; Lee, J. H.; et al. Artificial synapse based on a δ-FAPbI₃/atomic-layer-deposited SnO₂ bilayer memristor. *Nano. Lett.* **2024**, *24*, 4869-76. DOI
69. Li, R.; Li, N.; Hou, J.; et al. Aquatic environment remediation by atomic layer deposition-based multi-functional materials: a review. *J. Hazard. Mater.* **2021**, *402*, 123513. DOI

-
70. Richey, N. E.; de, Paula, C.; Bent, S. F. Understanding chemical and physical mechanisms in atomic layer deposition. *J. Chem. Phys.* **2020**, *152*, 040902. [DOI](#)
71. Jan, A.; Tanis-Kanbur, M. B.; Rietveld, L. C.; Heijman, S. G. J. A review on atomically modified materials by atomic layer deposition for wastewater treatment. *Open. Ceram.* **2025**, *22*, 100780. [DOI](#)
72. Yarbrough, J.; Shearer, A. B.; Bent, S. F. Next generation nanopatterning using small molecule inhibitors for area-selective atomic layer deposition. *J. Vac. Sci. Technol. A* **2021**, *39*, 021002. [DOI](#)
73. Paek, S.; Schouwink, P.; Athanasopoulou, E. N.; et al. From nano- to micrometer scale: the role of antisolvent treatment on high performance perovskite solar cells. *Chem. Mater.* **2017**, *29*, 3490-8. [DOI](#)
74. Ma, Y.; Liu, C.; Zhang, M.; Mai, Y. Review on the effects of solvent physical properties on the performance of slot-die coated perovskite solar cells. *Surf. Sci. Technol.* **2024**, *2*, 25. [DOI](#)
75. Taylor, A. D.; Sun, Q.; Goetz, K. P.; et al. A general approach to high-efficiency perovskite solar cells by any antisolvent. *Nat. Commun.* **2021**, *12*, 1878. [DOI](#) [PubMed](#) [PMC](#)
76. Nattoo, C. A.; Peña, T.; Nassiri, Nazif, K.; et al. Optoelectronic properties of atomic layer deposited and sputtered MoS₂ films. *ACS. Appl. Mater. Interfaces* **2025**, *17*, 47347-54. [DOI](#)
77. Zhao, W.; Duan, Y. Advanced applications of atomic layer deposition in perovskite-based solar cells. *Adv. Photonics. Res.* **2021**, *2*, 2100011. [DOI](#)
78. Armstrong, C.; Delumeau, L. V.; Muñoz-Rojas, D.; et al. Tuning the band gap and carrier concentration of titania films grown by spatial atomic layer deposition: a precursor comparison. *Nanoscale. Adv.* **2021**, *3*, 5908-18. [DOI](#) [PubMed](#) [PMC](#)
79. Dutta, T.; Yadav, N.; Wu, Y.; et al. Electronic properties of 2D materials and their junctions. *Nano. Mater. Sci.* **2024**, *6*, 1-23. [DOI](#)
80. Nguyen, C. T.; Cho, E. H.; Gu, B.; et al. Gradient area-selective deposition for seamless gap-filling in 3D nanostructures through surface chemical reactivity control. *Nat. Commun.* **2022**, *13*, 7597. [DOI](#) [PubMed](#) [PMC](#)
81. Choi, D. W.; Maeng, W. J.; Park, J. S. The conducting tin oxide thin films deposited via atomic layer deposition using tetrakis-dimethylamino tin and peroxide for transparent flexible electronics. *Appl. Surf. Sci.* **2014**, *313*, 585-90. [DOI](#)
82. Qiu, S.; Amaro, A.; Fabulyak, D.; et al. Impact of tetrakis(dimethylamido)tin(IV) degradation on atomic layer deposition of tin oxide films and perovskite solar cells. *Small* **2025**, *21*, 2404966. [DOI](#) [PubMed](#) [PMC](#)
83. Sheng, J.; Han, K. L.; Hong, T.; et al. Review of recent progresses on flexible oxide semiconductor thin film transistors based on atomic layer deposition processes. *J. Semicond.* **2018**, *39*, 011008. [DOI](#)
84. Hong, T.; Kim, H. W.; Kim, Y. S.; et al. Plasma-enhanced atomic layer deposition assisted low-temperature synthetic routes to rationally designed metastable C-axis aligned hexagonal In-Zn-O. *Chem. Mater.* **2023**, *35*, 5168-76. [DOI](#)
85. Lee, S.; Kim, M.; Mun, G.; et al. Effects of Al precursors on the characteristics of indium-aluminum oxide semiconductor grown by plasma-enhanced atomic layer deposition. *ACS. Appl. Mater. Interfaces* **2021**, *13*, 40134-44. [DOI](#)
86. Wang, C.; Zhao, D.; Grice, C. R.; et al. Low-temperature plasma-enhanced atomic layer deposition of tin oxide electron selective layers for highly efficient planar perovskite solar cells. *J. Mater. Chem. A* **2016**, *4*, 12080-7. [DOI](#)
87. Wang, H.; Zhao, Y.; Wang, Z.; et al. Hermetic seal for perovskite solar cells: an improved plasma enhanced atomic layer deposition encapsulation. *Nano. Energy* **2020**, *69*, 104375. [DOI](#)
88. Preischel, F.; Zanders, D.; Berning, T.; et al. Interplay of precursor and plasma for the deposition of HfO₂ via PEALD: film growth and dielectric properties. *Adv. Mater. Interfaces* **2023**, *10*, 2300244. [DOI](#)
89. Xu, L.; Zhang, Z.; Yang, L.; Yang, J.; Wang, P.; Gao, G.; et al. Comparison of thermal, plasma-enhanced and layer by layer Ar plasma treatment atomic layer deposition of tin oxide thin films. *J. Cryst. Growth* **2021**, *572*, 126264. [DOI](#)
90. Oviroh, P. O.; Akbarzadeh, R.; Pan, D.; Coetzee, R. A. M.; Jen, T. C. New development of atomic layer deposition: processes, methods and applications. *Sci. Technol. Adv. Mater.* **2019**, *20*, 465-96. [DOI](#) [PubMed](#) [PMC](#)
91. Sønsteby, H. H.; Yanguas-Gil, A.; Elam, J. W. Consistency and reproducibility in atomic layer deposition. *J. Vac. Sci. Technol. A* **2020**, *38*, 020804. [DOI](#)
92. Poodt, P.; Cameron, D. C.; Dickey, E.; et al. Spatial atomic layer deposition: a route towards further industrialization of atomic layer deposition. *J. Vac. Sci. Technol. A* **2012**, *30*, 010802. [DOI](#)
93. Asgarimoghaddam, H.; Chen, Q.; Ye, F.; Shahin, A.; Song, B.; Musselman, K. P. Zinc aluminum oxide encapsulation layers for perovskite solar cells deposited using spatial atomic layer deposition. *Small. Methods* **2024**, *8*, 2300995. [DOI](#) [PubMed](#)
94. Yersak, A. S.; Sharma, K.; Wallas, J. M.; Dameron, A. A.; Li, X.; Yang, Y.; et al. Spatial atomic layer deposition for coating flexible porous Li-ion battery electrodes. *J. Vac. Sci. Technol. A* **2018**, *36*, 01A123. [DOI](#)
95. Muñoz-Rojas, D.; MacManus-Driscoll, J. Spatial atmospheric atomic layer deposition: a new laboratory and industrial tool for low-cost photovoltaics. *Mater. Horiz.* **2014**, *1*, 314-20. [DOI](#)
96. Vale, J. P.; Sekkat, A.; Gheorghin, T.; et al. Can we rationally design and operate spatial atomic layer deposition systems for steering the growth regime of thin films? *J. Phys. Chem. C* **2023**, *127*, 9425-36. [DOI](#)

-
97. Jiang, X.; Shan, B.; Ma, G.; et al. Scalable deposition of SnO₂ ETL via SALD for large-area inverted perovskite solar modules. *Chem. Eng. J.* **2025**, *505*, 159629. DOI
98. Qian, J.; Xu, B.; Tian, W. A comprehensive theoretical study of halide perovskites ABX₃. *Org. Electron.* **2016**, *37*, 61–73. DOI
99. Li, C.; Lu, X.; Ding, W.; Feng, L.; Gao, Y.; Guo, Z. Formability of ABX₃ (X = F, Cl, Br, I) halide perovskites. *Acta. Cryst. B. Struct. Sci.* **2008**, *64*, 702–7. DOI
100. Sato, T.; Takagi, S.; Deledda, S.; Hauback, B. C.; Orimo, S. I. Extending the applicability of the Goldschmidt tolerance factor to arbitrary ionic compounds. *Sci. Rep.* **2016**, *6*, 23592. DOI PubMed PMC
101. Teo, S. H.; Ng, C. H.; Ng, Y. H.; Islam, A.; Hayase, S.; Taufiq-Yap, Y. H. Resolve deep-rooted challenges of halide perovskite for sustainable energy development and environmental remediation. *Nano. Energy.* **2022**, *99*, 107401. DOI
102. Meloni, S.; Palermo, G.; Ashari-Astani, N.; Grätzel, M.; Rothlisberger, U. Valence and conduction band tuning in halide perovskites for solar cell applications. *J. Mater. Chem. A.* **2016**, *4*, 15997–6002. DOI
103. Kusuma, F. J.; Widianto, E.; Wahyono, .; et al. Direct band gap prediction of single and double perovskite using cost-sensitive ensemble learning. *J. Alloys. Compd.* **2025**, *1037*, 182102. DOI
104. Ko, P. K.; Ge, J.; Ding, P.; et al. The deepest blue: major advances and challenges in deep blue emitting quasi-2D and nanocrystalline perovskite LEDs. *Adv. Mater.* **2025**, *37*, 2407764. DOI PubMed PMC
105. Ji, L.; Zhang, X.; Zhang, T.; et al. Band alignment of Pb-Sn mixed triple cation perovskites for inverted solar cells with negligible hysteresis. *J. Mater. Chem. A.* **2019**, *7*, 9154–62. DOI
106. Chen, L.; Yoo, J. W.; Hu, M.; Lee, S. U.; Seok, S. I. Intrinsic phase stability and inherent bandgap of formamidinium lead triiodide perovskite single crystals. *Angew. Chem. Int. Ed.* **2022**, *61*, e202212700. DOI PubMed
107. Kaiser, W.; Hussain, K.; Singh, A.; et al. Defect formation and healing at grain boundaries in lead-halide perovskites. *J. Mater. Chem. A.* **2022**, *10*, 24854–65. DOI
108. Guo, Z.; Wang, J.; Yin, W. J. Atomistic origin of lattice softness and its impact on structural and carrier dynamics in three dimensional perovskites. *Energy. Environ. Sci.* **2022**, *15*, 660–71. DOI
109. Liu, Y.; Lv, W.; Feng, J.; et al. Emerging thermochromic perovskite materials: insights into fundamentals, recent advances and applications. *Adv. Funct. Mater.* **2024**, *34*, 2402234. DOI
110. Wang, F.; Bai, S.; Tress, W.; Hagfeldt, A.; Gao, F. Defects engineering for high-performance perovskite solar cells. *NPJ. Flex. Electron.* **2018**, *2*, 22. DOI
111. Baumann, F.; Raga, S. R.; Lira-Cantú, M. Monitoring the stability and degradation mechanisms of perovskite solar cells by in situ and operando characterization. *APL. Energy.* **2023**, *1*, 011501. DOI
112. Wąsiak-Maciejak, A.; Przypis, L.; Żuraw, W.; et al. Compositional and interfacial engineering for improved light stability of flexible wide-bandgap perovskite solar cells. *J. Mater. Chem. A.* **2025**, *13*, 7335–46. DOI
113. Wang, H.; Zhang, Z.; Wang, X.; Duan, L.; Luo, J. Phenyltrimethylammonium chloride additive for highly efficient and stable FAPbI₃ perovskite solar cells. *Nano. Energy.* **2024**, *123*, 109423. DOI
114. Heo, D. Y.; Jang, W. J.; Jeong, M. J.; Noh, J. H.; Kim, S. Y. Optimal solvents for interfacial solution engineering of perovskite solar cells. *Sol. RRL.* **2022**, *6*, 2200485. DOI
115. Xu, C.; Hang, P.; Kan, C.; Guo, X.; Song, X.; Xu, C.; et al. Molecular ferroelectric self-assembled interlayer for efficient perovskite solar cells. *Nat. Commun.* **2025**, *16*, 835. DOI PubMed PMC
116. Li, S.; Li, X.; Dai, C.; He, W.; Shabdan, Y.; Guli, M. Research on the application of metal oxide buffer layers in perovskite solar cells. *Chem. Eng. J.* **2025**, *521*, 166935. DOI
117. Park, H.; Jeong, S.; Kim, E.; Shin, S.; Shin, H. Hole-transporting vanadium-containing oxide (V₂O_{5,x}) interlayers enhance stability of α-FAPbI₃-based perovskite solar cells (~23%). *ACS. Appl. Mater. Interfaces.* **2022**, *14*, 42007–17. DOI
118. Dong, J.; Jia, J.; Shi, B.; Feng, X.; Wu, Y.; Lv, P.; et al. Cr₂O₃ interlayer at TiO₂/perovskite interface propelling the efficiency improvement of perovskite solar cells. *Surf. Interfaces.* **2022**, *29*, 101761. DOI
119. Li, H.; Gao, B.; Yang, L.; et al. Magnesium oxide buffer layer for over 32% efficiency four-terminal perovskite/silicon tandem solar cells. *Adv. Energy. Mater.* **2025**, *15*, 2501762. DOI
120. Moumen, A.; Kumarage, G. C.; Comini, E. P-type metal oxide semiconductor thin films: synthesis and chemical sensor applications. *Sensors* **2022**, *22*, 1359. DOI PubMed PMC
121. Valadi, K.; Gharibi, S.; Taheri-Ledari, R.; Akin, S.; Maleki, A.; Shalan, A. E. Metal oxide electron transport materials for perovskite solar cells: a review. *Environ. Chem. Lett.* **2021**, *19*, 2185–207. DOI
122. Zhou, G.; Luo, X.; Wang, Z.; et al. Recent progress on cross-linkable fullerene-based electron transport materials for perovskite solar cells. *ChemSusChem* **2025**, *18*, e202401629. DOI

-
123. Kim, K.; Kim, M.; Lee, H.; Chung, D. W.; Kim, J. Multi-functional PEDOT:PSS as the efficient perovskite solar cells. *Small* **2024**, *20*, 2402341. DOI
124. Arumugam, G. M.; Karunakaran, S. K.; Liu, C.; et al. Inorganic hole transport layers in inverted perovskite solar cells: a review. *Nano. Select.* **2021**, *2*, 1081-116. DOI
125. Murugan, P.; Hu, T.; Hu, X.; Chen, Y. Advancements in organic small molecule hole-transporting materials for perovskite solar cells: past and future. *J. Mater. Chem. A* **2022**, *10*, 5044-81. DOI
126. Althumayri, M.; Das, R.; Banavath, R.; Beker, L.; Achim, A. M.; Ceylan, Koydemir. H. Recent advances in transparent electrodes and their multimodal sensing applications. *Adv. Sci.* **2024**, *11*, 2405099. DOI PubMed PMC
127. Wang, C.; Li, J.; Luo, C.; et al. SnO₂-based resistive hydrogen gas sensor: a comprehensive review from performance to function optimization. *Mater. Sci. Semicond. Process.* **2025**, *188*, 109209. DOI
128. Phogat, P.; Jha, R.; Singh, S. Harnessing ZnO morphologies in energy application and sustainable development. *Phys. Scr.* **2024**, *99*, 102004. DOI
129. Chen, K. T.; Hsu, C. H.; Ren, F. B.; et al. Influence of annealing temperature of nickel oxide as hole transport layer applied for inverted perovskite solar cells. *J. Vac. Sci. Technol. A* **2021**, *39*, 062401. DOI
130. Patel, V. D.; Gupta, D. Solution-processed metal-oxide based hole transport layers for organic and perovskite solar cell: a review. *Mater. Today. Commun.* **2022**, *31*, 103664. DOI
131. Wu, S.; Liu, M.; Jen, A. K. Y. Prospects and challenges for perovskite-organic tandem solar cells. *Joule* **2023**, *7*, 484-502. DOI
132. Szabó, G.; Kamat, P. V. Spiro-OMeTAD: unique redox chemistry driving the hole transport. *ACS. Energy. Lett.* **2024**, *10*, 330-6. DOI
133. Duan, Y.; Chen, Y.; Wu, Y.; Liu, Z.; Liu, S.; Peng, Q. A comprehensive review of organic hole-transporting materials for highly efficient and stable inverted perovskite solar cells. *Adv. Funct. Mater.* **2024**, *34*, 2315604. DOI
134. Ouedraogo, N. A. N.; Odunmbaku, G. O.; Guo, B.; et al. Oxidation of spiro-OMeTAD in high-efficiency perovskite solar cells. *ACS. Appl. Mater. Interfaces.* **2022**, *14*, 34303-27. DOI
135. Ahmad, N.; Yuan, J.; Zou, Y. One more step towards better stability of non-fullerene organic solar cells: advances, challenges, future perspectives, and the era of artificial intelligence. *Energy. Environ. Sci.* **2025**, *18*, 5093-158. DOI
136. Kim, S.; Lee, S. H.; Jo, I. H.; Park, T. J.; Kim, J. H. Reduced leakage current in atomic-layer-deposited HfO₂ thin films deposited at low temperature by in situ defect passivation. *Appl. Surf. Sci.* **2024**, *645*, 158790. DOI
137. Yao, Q.; Song, H.; Zhang, M.; et al. Recent advances in semi-transparent perovskite solar cells: fabrication, structural engineering, applications, and future challenges. *J. Mater. Chem. C* **2025**, *13*, 22059-103. DOI
138. Chen, R.; Zhang, W.; Guan, X.; et al. Rear electrode materials for perovskite solar cells. *Adv. Funct. Mater.* **2022**, *32*, 2200651. DOI
139. Brinkmann, K. O.; Gahlmann, T.; Riedl, T. Atomic layer deposition of functional layers in planar perovskite solar cells. *Sol. RRL* **2020**, *4*, 1900332. DOI
140. Kim, B. J.; Jang, J. H.; Kim, J.; Oh, K. S.; Choi, E. Y.; Park, N. Efficiency and stability enhancement of organic-inorganic perovskite solar cells through micropatterned Norland optical adhesive and polyethylene terephthalate encapsulation. *Mater. Today. Commun.* **2019**, *20*, 100537. DOI
141. Wang, Y.; Ahmad, I.; Leung, T.; et al. Encapsulation and stability testing of perovskite solar cells for real life applications. *ACS. Mater. Au* **2022**, *2*, 215-36. DOI PubMed PMC
142. Lv, Y.; Xu, P.; Ren, G.; et al. Low-temperature atomic layer deposition of metal oxide layers for perovskite solar cells with high efficiency and stability under harsh environmental conditions. *ACS. Appl. Mater. Interfaces.* **2018**, *10*, 23928-37. DOI
143. Allen, O. J.; Kang, J.; Qian, S.; Hinsch, J. J.; Zhang, L.; Wang, Y. A theoretical review of passivation technologies in perovskite solar cells. *Energy. Mater.* **2024**, *4*, 400037. DOI
144. Lin, L.; Jones, T. W.; Yang, T. C. J.; et al. Hydrogen bonding in perovskite solar cells. *Matter* **2024**, *7*, 38-58. DOI
145. Walsh, A.; Yan, Y.; Huda, M. N.; Al-Jassim, M. M.; Wei, S. H. Band edge electronic structure of BiVO₄: elucidating the role of the Bi s and V d orbitals. *Chem. Mater.* **2009**, *21*, 547-51. DOI
146. Wang, Y.; Ba, Z.; Dong, S.; Xie, W.; Wu, Z.; Ran, C. Advancing SnO₂ electron transport layer for efficient perovskite photovoltaics: a critical review. *ACS. Appl. Mater. Interfaces.* **2025**, *17*, 27651-70. DOI PubMed
147. Bae, D.; Kwon, S.; Oh, J.; Kim, W. K.; Park, H. Investigation of Al₂O₃ diffusion barrier layer fabricated by atomic layer deposition for flexible Cu(In,Ga)Se₂ solar cells. *Renew. Energy* **2013**, *55*, 62-8. DOI
148. Cochran, E. A.; Woods, K. N.; Johnson, D. W.; Page, C. J.; Boettcher, S. W. Unique chemistries of metal-nitrate precursors to form metal-oxide thin films from solution: materials for electronic and energy applications. *J. Mater. Chem. A* **2019**, *7*, 24124-49. DOI
149. Sharma, B.; Satapathi, S. Semi-transparent perovskite solar cells for building integrated photovoltaics application. *Adv. Mater. Technol.* **2025**, *10*, e00434. DOI

-
150. Kim, J.; Kim, Y. S.; Choi, J. Y.; Lee, Y. H.; Kong, Y. M.; Kim, D. The electrical, optical, heating property and electromagnetic wave shield effect of TiO₂/Ag/TiO₂ thin films. *Korean. J. Met. Mater.* **2024**, *62*, 735-9. [DOI](#)
151. Miglani, A.; Ogale, S. B.; Game, O. S. Architectural innovations in perovskite solar cells. *Small* **2025**, *21*, 2411355. [DOI PubMed](#)
152. Girtan, M.; Negulescu, B. A review on oxide/metal/oxide thin films on flexible substrates as electrodes for organic and perovskite solar cells. *Opt. Mater. X* **2022**, *13*, 100122. [DOI](#)
153. Deschermeier, R.; Rehfeldt, S.; Klein, H. Method for characterization of solvents for physical absorption processes. *Chem. Eng. Technol.* **2017**, *40*, 28-38. [DOI](#)
154. Yu, X.; Sun, X.; Zhu, Z.; Li, Z. A. Stabilization strategies of buried interface for efficient SAM-based inverted perovskite solar cells. *Angew. Chem. Int. Ed.* **2025**, *64*, e202419608. [DOI](#)
155. Tang, H.; Shen, Z.; Shen, Y.; et al. Reinforcing self-assembly of hole transport molecules for stable inverted perovskite solar cells. *Science* **2024**, *383*, 1236-40. [DOI](#)
156. Kan, Z.; Wang, Z.; Firdaus, Y.; Babics, M.; Alshareef, H. N.; Beaujuge, P. M. Atomic-layer-deposited AZO outperforms ITO in high-efficiency polymer solar cells. *J. Mater. Chem. A* **2018**, *6*, 10176-83. [DOI](#)
157. Kruszyńska, J.; Ostapko, J.; Ozkaya, V.; et al. Atomic layer engineering of aluminum-doped zinc oxide films for efficient and stable perovskite solar cells. *Adv. Mater. Interfaces* **2022**, *9*, 2200575. [DOI](#)
158. Chouhan, A. S.; Jasti, N. P.; Avasthi, S. The dual role of ozone-treated aluminum doped zinc oxide for CH₃NH₃PbI₃ solar cells. *Org. Electron.* **2019**, *66*, 249-57. [DOI](#)
159. Melo Monteiro Modesto AP, Merlo RB, Guzman DG, Barros TA, dos Santos TEA, Marques FC. Properties of AZO films grown by ALD applied as a TCO layer in perovskite solar cells. *MRS. Adv.* **2024**, *9*, 916-20. [DOI](#)
160. Vijayaraghavan, S.; Wall, J.; Li, L.; Xing, G.; Zhang, Q.; Yan, F. Low-temperature processed highly efficient hole transport layer free carbon-based planar perovskite solar cells with SnO₂ quantum dot electron transport layer. *Mater. Today. Phys.* **2020**, *13*, 100204. [DOI](#)
161. Shekargoftar, M.; Pospisil, J.; Kratochvíl, M.; Vida, J.; Souček, P.; Homola, T. Low-temperature and rapid deposition of an SnO₂ layer from a colloidal nanoparticle dispersion for use in planar perovskite solar cells. *Energy. Technol.* **2021**, *9*, 2001076. [DOI](#)
162. Hsu, C. H.; Chen, K. T.; Lin, L. Y.; et al. Tantalum-doped TiO₂ prepared by atomic layer deposition and its application in perovskite solar cells. *Nanomaterials* **2021**, *11*, 1504. [DOI PubMed PMC](#)
163. Chai, W.; Zhu, W.; Chen, D.; et al. Low-temperature preparation of titanium dioxide thin layer for highly efficient CsPbI₃ perovskite solar cells. *Mater. Today. Energy.* **2023**, *37*, 101410. [DOI](#)
164. Vincent, T.; Coutancier, D.; Dally, P.; et al. Fine tuning of Nb-incorporated TiO₂ thin films by atomic layer deposition and application as efficient electron transport layer in perovskite solar cells. *J. Vac. Sci. Technol. A* **2024**, *42*, 032802. [DOI](#)
165. Kam, M.; Zhang, Q.; Zhang, D.; Fan, Z. Room-temperature sputtered SnO₂ as robust electron transport layer for air-stable and efficient perovskite solar cells on rigid and flexible substrates. *Sci. Rep.* **2019**, *9*, 6963. [DOI PubMed PMC](#)
166. Muthukrishnan, A. P.; Lee, J.; Kim, J.; Kim, C. S.; Jo, S. Low-temperature solution-processed SnO₂ electron transport layer modified by oxygen plasma for planar perovskite solar cells. *RSC. Adv.* **2022**, *12*, 4883-90. [DOI PubMed PMC](#)
167. Min, H.; Lee, D. Y.; Kim, J.; et al. Perovskite solar cells with atomically coherent interlayers on SnO₂ electrodes. *Nature* **2021**, *598*, 444-50. [DOI](#)
168. Seo, G.; Yoo, J. J.; Nam, S.; et al. Efficient and luminescent perovskite solar cells using defect-suppressed SnO₂ via excess ligand strategy. *Nat. Energy.* **2025**, *10*, 774-84. [DOI](#)
169. Uddin, A.; Yi, H. Progress and challenges of SnO₂ electron transport layer for perovskite solar cells: a critical review. *Sol. RRL.* **2022**, *6*, 2100983. [DOI](#)
170. Lee, J. H.; Lee, S.; Kim, T.; et al. Interfacial α -FAPbI₃ phase stabilization by reducing oxygen vacancies in SnO_{2-x}. *Joule* **2023**, *7*, 380-97. [DOI](#)
171. Mattinen, M.; Gity, F.; Coleman, E.; et al. Atomic layer deposition of large-area polycrystalline transition metal dichalcogenides from 100 °C through control of plasma chemistry. *Chem. Mater.* **2022**, *34*, 7280-92. [DOI PubMed PMC](#)
172. Liu, J.; Li, S.; Liu, S.; et al. Oxygen vacancy management for high-temperature mesoporous SnO₂ electron transport layers in printable perovskite solar cells. *Angew. Chem. Int. Ed.* **2022**, *61*, e202202012. [DOI](#)
173. Martinez-Puente, M. A.; Tirado, J.; Jaramillo, F.; et al. Unintentional hydrogen incorporation into the SnO₂ electron transport layer by ALD and its effect on the electronic band structure. *ACS. Appl. Energy. Mater.* **2021**, *4*, 10896-908. [DOI](#)
174. Gong, J.; Song, M.; Kim, Y. K.; Kim, G. M. Unveiling and optimizing the role of ALD-SnO₂ in perovskite solar cells. *Adv. Ind. Eng. Chem.* **2025**, *1*, 10. [DOI](#)
175. Zhang, X.; Zhou, Y.; Chen, M.; et al. Novel bilayer SnO₂ electron transport layers with atomic layer deposition for high-performance α -FAPbI₃ perovskite solar cells. *Small* **2023**, *19*, 2303254. [DOI](#)

-
176. Ge, Y.; Zheng, L.; Wang, H.; et al. Suppressing wide-angle light loss and non-radiative recombination for efficient perovskite solar cells. *Nat. Photonics*. **2025**, *19*, 170-7. DOI
177. Chen, X.; Yuan, Z.; Fan, S.; et al. Enhanced light transmittance of electron transport layer through bilayer SnO₂ for high-performance semitransparent perovskite solar cells. *ChemSusChem* **2025**, *18*, e202402582. DOI
178. Gesesse, G. D.; Provost, M.; Yaiche, A.; et al. Innovative Nb-doped SnO₂ electron transport layers prepared by atomic layer deposition for enhanced perovskite solar cells. *ACS. Appl. Energy. Mater.* **2025**, *8*, 5421-30. DOI
179. Ko, D.; Joo, S. H.; Kim, S.; Kim, I. S.; Park, M. Low-temperature photocrystallization of atomic layer deposition-processed tin oxide for highly efficient and flexible perovskite solar cells. *Small. Sci.* **2025**, *5*, 2500196. DOI PubMed PMC
180. Lee, J. W.; Adu, J. S.; Agbenyeke, R. E.; et al. Ultrathin oxygen deficient SnO_x films as electron extraction layers for perovskite solar modules. *J. Mater. Chem. A*. **2025**, *13*, 4100-6. DOI
181. Cheng, Y.; Yang, Q. D.; Xiao, J.; et al. Decomposition of organometal halide perovskite films on zinc oxide nanoparticles. *ACS. Appl. Mater. Interfaces*. **2015**, *7*, 19986-93. DOI
182. Tsarev, S.; Olthof, S.; Boldyreva, A. G.; Aldoshin, S. M.; Stevenson, K. J.; Troshin, P. A. Reactive modification of zinc oxide with methylammonium iodide boosts the operational stability of perovskite solar cells. *Nano. Energy*. **2021**, *83*, 105774. DOI
183. Fournier, O.; Bapaume, C. D.; Messou, D.; et al. Chemical passivation with phosphonic acid derivatives of ZnO deposited by atomic layer deposition and its influence on the halide perovskite interface. *ACS. Appl. Energy. Mater.* **2021**, *4*, 5787-97. DOI
184. Su, Z.; Xu, D.; Ma, Q.; et al. Atomic layer deposited ZnO-SnO₂ electron transport bilayer for wide-bandgap perovskite solar cells. *Sol. RRL*. **2023**, *7*, 2201026. DOI
185. Khan, F.; Ahmad, V.; Alshahrani, T.; Balobaid, A. S.; Alanazi, A. M. Influence of Al doping in zinc oxide electron transport layer for the degradation triple-cation-based organometal halide perovskite solar cells. *Heliyon* **2023**, *9*, e16069. DOI PubMed PMC
186. El-Shishtawy, R. M.; ElShishtawy, N. Perovskite solar cells: organic-based molecules for electron and hole transport materials with machine learning insights. *Curr. Opin. Colloid. Interface. Sci.* **2024**, *74*, 101848. DOI
187. Rakheja, B.; Hultqvist, A.; Varma, R. M.; et al. Interfacial chemistry between formamidinium lead trihalide perovskites and atomic-layer-deposited tin oxide. *ACS. Appl. Energy. Mater.* **2025**, *8*, 8467-78. DOI
188. Lu, H.; Gu, B.; Fang, S. In situ growth of an opal-like TiO₂ electron transport layer by atomic layer deposition for perovskite solar cells. *Sustain. Energy. Fuels*. **2021**, *5*, 880-5. DOI
189. Zimmermann, E.; Wong, K. K.; Seewald, T.; et al. Controlled crystallinity of TiO₂ layers grown by atmospheric pressure spatial atomic layer deposition and their impact on perovskite solar cell efficiency. *Int. J. Photoenergy*. **2022**, *2022*, 1172871. DOI
190. Erdenebileg, E.; Wang, H.; Li, J.; et al. Low-temperature atomic layer deposited electron transport layers for co-evaporated perovskite solar cells. *Sol. RRL*. **2022**, *6*, 2100842. DOI
191. Shin, S.; Park, S.; Bae, Y. H.; Noh, J. S. Rational tuning of SnO₂ electron transport layer grown by atomic layer deposition for performance improvement of perovskite solar cells. *Sol. Energy*. **2024**, *277*, 112754. DOI
192. Fei, F.; Liao, Y.; Xu, Y.; et al. Stable inverted perovskite solar cells with efficiency over 23.0% via dual-layer SnO₂ on perovskite. *ACS. Appl. Mater. Interfaces*. **2024**, *16*, 24760-70. DOI
193. Farva, U.; Lee, H. W.; Kim, R. N.; Lee, D. G.; Kang, D. W.; Kim, J. Growth temperature influence on atomic-layer-deposited In₂O₃ thin films and their application in inorganic perovskite solar cells. *Nanomaterials* **2021**, *11*, 2047. DOI PubMed PMC
194. Afraj, S. N.; Velusamy, A.; Sharma, S.; et al. Recent progress in molecularly tailored organic hole transporting materials for highly efficient perovskite solar cells. *J. Mater. Chem. C*. **2025**, *13*, 15234-89. DOI
195. Ouyang, D.; Huang, Z.; Choy, W. C. Solution-processed metal oxide nanocrystals as carrier transport layers in organic and perovskite solar cells. *Adv. Funct. Mater.* **2019**, *29*, 1804660. DOI
196. Gawlińska-Nęcek, K.; Starowicz, Z.; Janusz-Skuza, M.; Jarzębska, A.; Panek, P. The copper oxide with alkali potassium dopant for heterojunction solar cells application. *Electron. Mater. Lett.* **2024**, *20*, 548-56. DOI
197. Kumar, A.; Singh, S.; Yadav, A. Recent progress in inverted perovskite solar cells employing nickel oxide (NiO_x) as a hole transport materials. *Mater. Today. Proc.* **2021**, *46*, 5827-32. DOI
198. Gao, M.; Ou, Z.; Wang, C.; et al. Multifunctional buried molecule-bridge for high-performance inverted perovskite solar cells. *Adv. Mater.* **2026**, *38*, e14273. DOI
199. Park, H.; Nandi, P.; In, Y.; Shin, H. Practical and thermal atomic layer deposition of NiO as hole-transporting layers for inverted perovskite solar cells. *Sol. RRL*. **2024**, *8*, 2300858. DOI
200. Phung, N.; Verheijen, M.; Todinova, A.; et al. Enhanced self-assembled monolayer surface coverage by ALD NiO in pin perovskite solar cells. *ACS. Appl. Mater. Interfaces*. **2021**, *14*, 2166-76. DOI PubMed PMC
201. Jia, X.; Chang, Z.; Wang, K.; et al. Hydroxyl-functionalized ultrathin NiO_x interlayer for minimized energy loss and enhanced interface stability in perovskite photovoltaics. *J. Mater. Chem. A*. **2025**, *13*, 29983-93. DOI

-
202. He, J.; Li, G.; Huang, G.; et al. Improved anchoring of self-assembled monolayer on hydroxylated NiO_x film surface for efficient and stable inverted perovskite solar cells. *Adv. Funct. Mater.* **2025**, *35*, 2413104. [DOI](#)
203. Xu, Y.; Wang, C.; Amornkitbamrung, U.; et al. Molecular bridge on buried interface for energy level alignment in inverted perovskite solar cell with efficiency over 25%. *ACS. Energy. Lett.* **2025**, *10*, 3407-14. [DOI](#)
204. Pellegrino, A. L.; Lo, Presti. F.; Smecca, E.; et al. A low temperature growth of Cu₂O thin films as hole transporting material for perovskite solar cells. *Materials* **2022**, *15*, 7790. [DOI](#) [PubMed](#) [PMC](#)
205. Weiß, A.; Goldmann, J.; Kettunen, S.; et al. Conversion of ALD CuO thin films into transparent conductive p-type CuI thin films. *Adv. Mater. Interfaces.* **2023**, *10*, 2201860. [DOI](#)
206. Sun, Q.; Sadhu, A.; Lie, S.; Wong, L. H. Critical review of Cu-based hole transport materials for perovskite solar cells: from theoretical insights to experimental validation. *Adv. Mater.* **2024**, *36*, 2402412. [DOI](#) [PubMed](#)
207. Farva, U.; Kim, J. Temperature optimization of NiO hole transport layer prepared by atomic layer deposition. *Vacuum* **2023**, *207*, 111674. [DOI](#)
208. Phung, N.; Zhang, D.; van, Helvoirt. C.; et al. Atomic layer deposition of NiO applied in a monolithic perovskite/PERC tandem cell. *Sol. Energy. Mater. Sol. Cells.* **2023**, *261*, 112498. [DOI](#)
209. Xu, Y.; Park, H.; Amornkitbamrung, U.; et al. Synergistic passivation of pyridinium tetrafluoroborate (PyBF₄) in inverted (CsPbI₃)_{0.05}(FAPbI₃)_{1-x}(MAPbBr₃)_{0.95} solar cells with atomic layer deposited NiO layers. *Sol. RRL.* **2025**, *9*, 2400765. [DOI](#)
210. Zhu, Z.; Yuan, S.; Mao, K.; et al. Low-temperature atomic layer deposition of hole transport layers for enhanced performance and scalability in textured perovskite/silicon tandem solar cells. *Adv. Energy. Mater.* **2024**, *14*, 2402365. [DOI](#)
211. Cho, A. N.; Park, N. G. Impact of interfacial layers in perovskite solar cells. *ChemSusChem* **2017**, *10*, 3687-704. [DOI](#) [PubMed](#)
212. Shen, Y.; Deng, K.; Li, L. Spiro-OMeTAD-based hole transport layer engineering toward stable perovskite solar cells. *Small. Methods.* **2022**, *6*, 2200757. [DOI](#)
213. Xiang, W.; Liu, S.; Tress, W. Interfaces and interfacial layers in inorganic perovskite solar cells. *Angew. Chem. Int. Ed.* **2021**, *60*, 26644-57. [DOI](#) [PubMed](#)
214. Xu, R.; Wang, C.; Zhang, Z.; et al. Buried interface engineering: a key to unlocking the potential of self-assembled monolayer (SAM)-based inverted perovskite solar cells. *Small* **2025**, *21*, e2503114. [DOI](#)
215. Lee, J. W.; Kim, H. S.; Park, N. G. Lewis acid-base adduct approach for high efficiency perovskite solar cells. *Acc. Chem. Res.* **2016**, *49*, 311-9. [DOI](#) [PubMed](#)
216. Tong, H.; Li, F. F.; Du, M.; et al. Interface engineering, charge carrier dynamics, and solar-driven applications of halide perovskite/2D material heterostructured photocatalysts. *ACS. Appl. Mater. Interfaces.* **2025**, *17*, 23431-65. [DOI](#) [PubMed](#) [PMC](#)
217. Jiang, K.; Ma, Z.; Lan, J.; Chen, D.; Li, W.; Fan, J. Screening of functional small molecules via modified machine learning strategy toward efficient all-inorganic perovskite solar cells. *ACS. Appl. Mater. Interfaces.* **2024**, *16*, 31833-42. [DOI](#)
218. Chavan, R. D.; Parikh, N.; Tavakoli, M. M.; et al. Mesoscopic TiO₂/Nb₂O₅ electron transfer layer for efficient and stable perovskite solar cells. *Adv. Mater. Interfaces.* **2021**, *8*, 2100177. [DOI](#)
219. Zhao, R.; Zhang, K.; Zhu, J.; et al. Surface passivation of organometal halide perovskites by atomic layer deposition: an investigation of the mechanism of efficient inverted planar solar cells. *Nanoscale. Adv.* **2021**, *3*, 2305-15. [DOI](#) [PubMed](#) [PMC](#)
220. Yang, Y.; Cheng, S.; Zhu, X.; et al. Inverted perovskite solar cells with over 2,000 h operational stability at 85 °C using fixed charge passivation. *Nat. Energy.* **2024**, *9*, 37-46. [DOI](#)
221. Xing, Z.; Fan, B.; Meng, X.; et al. Repairing humidity-induced interfacial degradation in quasi-2D perovskite solar cells printed in ambient air. *Energy. Environ. Sci.* **2024**, *17*, 3660-9. [DOI](#)
222. Choi, D.; Shin, D.; Li, C.; et al. Carboxyl-functionalized perovskite enables ALD growth of a compact and uniform ion migration barrier. *Joule* **2025**, *9*, 101801. [DOI](#)
223. Ghosh, S.; Pariari, D.; Behera, T.; et al. Buried interface passivation of perovskite solar cells by atomic layer deposition of Al₂O₃. *ACS. Energy. Lett.* **2023**, *8*, 2058-65. [DOI](#)
224. Li, J.; Xing, Z.; Li, D.; et al. Suppressed ion migration in FA-rich perovskite photovoltaics through enhanced nucleation of encapsulation interface. *Small* **2024**, *20*, 2305732. [DOI](#)
225. Zhang, L.; Lu, W.; Ding, F.; Jin, R.; Wang, Q. Ultrathin ALD-SnO₂ interlayer for performance enhancement of inverted perovskite solar cells. *Mater. Today. Commun.* **2025**, *46*, 112921. [DOI](#)
226. Yadav, R. K.; Manjunath, V.; Kim, Y. T.; et al. Optimized rear-interface passivation of SnS thin-film solar cells using a controlled germanium oxide interlayer for enhanced photovoltaic performance. *Small* **2025**, *21*, e07626. [DOI](#)
227. Du, L.; Li, C.; Jiang, Y.; et al. Indium oxide buffer layer for perovskite/Si 4-terminal tandem solar cells with efficiency exceeding 30%. *J. Energy. Chem.* **2025**, *102*, 189-96. [DOI](#)

-
228. Seo, S.; Shin, S.; Kim, E.; Jeong, S.; Park, N. G.; Shin, H. Amorphous TiO₂ coatings stabilize perovskite solar cells. *ACS. Energy. Lett.* **2021**, *6*, 3332–41. [DOI](#)
229. Choi, E.; Lee, J. W.; Anaya, M.; et al. Synergetic effect of aluminum oxide and organic halide salts on two-dimensional perovskite layer formation and stability enhancement of perovskite solar cells. *Adv. Energy. Mater.* **2023**, *13*, 2301717. [DOI](#)
230. Zheng, Z.; Xue, Z.; Zhao, K.; et al. Unveiling and overcoming instabilities in perovskite solar cells induced by atomic-layer-deposition tin oxide. *Sol. RRL.* **2024**, *8*, 2301076. [DOI](#)
231. Yu, B.; Tang, F.; Yang, Y.; et al. Impermeable atomic layer deposition for sputtering buffer layer in efficient semi-transparent and tandem solar cells via activating unreactive substrate. *Adv. Mater.* **2023**, *35*, 2202447. [DOI](#)
232. Johnson, S. A.; White, K. P.; Tong, J.; et al. Improving the barrier properties of tin oxide in metal halide perovskite solar cells using ozone to enhance nucleation. *Joule* **2023**, *7*, 2873–93. [DOI](#)
233. Amornkitbamrung, U.; Xu, Y.; Gibson, A.; et al. Mechanically robust and yet electrically conductive C60-SnO₂ electron transporting bilayer in stable perovskite solar cells. *Langmuir* **2025**, *41*, 21500–8. [DOI](#)
234. Gupta, S.; Laxmi, L.; Chityala, V. G.; et al. Optimization of atomic layer deposition process of tin oxide thin films for near-infrared-transparent halide perovskite solar cells. *ACS. Appl. Energy. Mater.* **2025**, *8*, 10183–91. [DOI](#)
235. Lukas, T.; Seo, S.; Holzhey, P.; et al. Charge extraction multilayers enable positive-intrinsic-negative perovskite solar cells with carbon electrodes. *ACS. Energy. Lett.* **2025**, *10*, 2736–42. [DOI PubMed PMC](#)
236. Zhang, L.; Fang, M.; Fu, L. S.; et al. Ultrathin HfAlO ferroelectrics enhancing electron transport and perovskite solar cell performance. *J. Mater. Res.* **2021**, *36*, 1855–65. [DOI](#)
237. Yang, Y.; Zhang, Y.; Li, R.; et al. Low-temperature atomic layer deposition of double-layer water vapor barrier for high humidity stable perovskite solar cells. *Adv. Opt. Mater.* **2023**, *11*, 2300148. [DOI](#)
238. Guli, M.; Zhang, Y.; Li, R.; He, W.; Lan, C.; Zhou, Y. An impressive open-circuit voltage of 1.223 V and high humidity stability of perovskite solar cells with MgO buffer layer deposited by low-temperature atomic layer deposition. *Small* **2024**, *20*, 2404199. [DOI](#)
239. Witteck, R.; Nguyen, Minh. D.; Paul, G.; et al. Reducing thermal degradation of perovskite solar cells during vacuum lamination by internal diffusion barriers. *ACS. Appl. Energy. Mater.* **2024**, *7*, 10750–7. [DOI PubMed PMC](#)
240. Zardetto, V.; Williams, B. L.; Perrotta, A.; et al. Atomic layer deposition for perovskite solar cells: research status, opportunities and challenges. *Sustain. Energy. Fuels.* **2017**, *1*, 30–55. [DOI](#)
241. Haghighi, M.; Ghazyani, N.; Mahmoodpour, S.; et al. Low-temperature processing methods for tin oxide as electron transporting layer in scalable perovskite solar cells. *Sol. RRL.* **2023**, *7*, 2201080. [DOI](#)
242. Kuang, Y.; Zardetto, V.; van, Gils. R.; et al. Low-temperature plasma-assisted atomic-layer-deposited SnO₂ as an electron transport layer in planar perovskite solar cells. *ACS. Appl. Mater. Interfaces.* **2018**, *10*, 30367–78. [DOI PubMed PMC](#)
243. Yu, B.; Zhang, J.; Yang, Y.; Yu, D.; Mai, Y.; Chen, X. Influences of deposition conditions on atomic layer deposition films for enhanced performance in perovskite solar cells. *Energy. Mater.* **2024**, *4*, 400045. [DOI](#)
244. Zhang, Y.; Ding, Y.; Christofides, P. D. Multiscale computational fluid dynamics modeling and reactor design of plasma-enhanced atomic layer deposition. *Comput. Chem. Eng.* **2020**, *142*, 107066. [DOI](#)
245. Koushik, D.; Hazendonk, L.; Zardetto, V.; et al. Chemical analysis of the interface between hybrid organic-inorganic perovskite and atomic layer deposited Al₂O₃. *ACS. Appl. Mater. Interfaces.* **2019**, *11*, 5526–35. [DOI PubMed PMC](#)
246. Kunene T, Kwanda Tartibu L, Ukoba K, Jen TC. Review of atomic layer deposition process, application and modeling tools. *Mater. Today. Proc.* **2022**, *62*, S95–109. [DOI](#)
247. Mallik, N.; Hajhemati, J.; Dufoulon, V.; et al. Interfacial reactions between atomic layer deposited NiO_x hole transport layers and metal halide perovskites in nip perovskite solar cells. *EES. Solar.* **2025**, *1*, 1004–16. [DOI](#)
248. Apergi, S.; Brocks, G.; Tao, S.; Olthof, S. Probing the reactivity of ZnO with perovskite precursors. *ACS. Appl. Mater. Interfaces.* **2024**, *16*, 14984–94. [DOI PubMed PMC](#)
249. Yang, Y.; Wang, S.; Ji, W.; et al. TiCl₄ precursor affecting the performance of HTM-free carbon-based perovskite solar cell. *Nanotechnology* **2023**, *35*, 07LT01. [DOI](#)
250. Hiller, D.; Munnik, F.; López-Vidrier, J.; et al. Comparison of three titanium precursors for atomic-layer-deposited TiO₂ for passivating contacts on silicon. *J. Vac. Sci. Technol. A.* **2024**, *42*, 032406. [DOI](#)
251. Vazquez-Arce, J. L.; Suta, T.; Fodor, B.; et al. Optical properties of TiO₂ grown by atomic layer deposition using various oxidizing agents: the ellipsometry analysis of absorption properties. *Adv. Mater. Interfaces.* **2024**, *11*, 2400269. [DOI](#)
252. Lee, J. E.; Motti, S. G.; Oliver, R. D. J.; et al. Unraveling loss mechanisms arising from energy-level misalignment between metal halide perovskites and hole transport layers. *Adv. Funct. Mater.* **2024**, *34*, 2401052. [DOI](#)
253. Agresti, A.; Di, Giacomo. F.; Pescetelli, S.; Di, Carlo. A. Scalable deposition techniques for large-area perovskite photovoltaic technology: a multi-perspective review. *Nano. Energy.* **2024**, *122*, 109317. [DOI](#)

-
254. Chen, M.; Nijboer, M.; Kovalgin, A.; Nijmeijer, A.; Roozeboom, F.; Luiten-Olieman, M. Atmospheric-pressure atomic layer deposition: recent applications and new emerging applications in high-porosity/3D materials. *Dalton. Trans.* **2023**, 52, 10254–77. DOI PubMed PMC
255. Lisker, M.; Kalishettyhalli, Mahadevaiah. M.; Dorai, Swamy. Reddy. K. Plasma-enhanced atomic layer deposition of silicon nitride for front-end-of-line applications. *J. Vac. Sci. Technol. A* **2023**, 41, 042406. DOI
256. Riazimehr, S.; Esteki, A.; Otto, M.; et al. Plasma-enhanced atomic layer deposition of Al₂O₃ on graphene via an in situ-deposited interlayer. *Mater. Sci. Semicond. Process.* **2025**, 199, 109829. DOI
257. Hoye, R. L.; Muñoz-Rojas, D.; Sun, Z.; et al. Spatial atomic layer deposition for energy and electronic devices. *PRX. Energy*. **2025**, 4, 017002. DOI
258. Musselman, K. P.; Uzoma, C. F.; Miller, M. S. Nanomanufacturing: high-throughput, cost-effective deposition of atomic scale thin films via atmospheric pressure spatial atomic layer deposition. *Chem. Mater.* **2016**, 28, 8443–52. DOI
259. Yan, G.; Huang, G.; Shi, J.; et al. A review on reactor design and surface modification of atomic layer deposition for functional nanoparticles. *Adv. Mater. Interfaces*. **2025**, 12, e00140. DOI

Disclaimer/Publisher’s Note: All statements, opinions, and data contained in this publication are solely those of the individual author(s) and contributor(s) and do not necessarily reflect those of OAE and/or the editor(s). OAE and/or the editor(s) disclaim any responsibility for harm to persons or property resulting from the use of any ideas, methods, instructions, or products mentioned in the content.



© The Author(s) 2026. Open Access This article is licensed under a Creative Commons Attribution 4.0 International License (<https://creativecommons.org/licenses/by/4.0/>), which permits unrestricted use, sharing, adaptation, distribution and reproduction in any medium or format, for any purpose, even commercially, as long as you give appropriate credit to the original author(s) and the source, provide a link to the Creative Commons license, and indicate if changes were made.